AIP | Chaos
An Interdisciplinary Journal of Nonlinear Science
25TH ANNIVERSARY

The joint space-time statistics of macroweather precipitation, space-time statistical factorization and macroweather models

S. Lovejoy and M. I. P. de Lima

Citation: Chaos **25**, 075410 (2015); doi: 10.1063/1.4927223
View online: http://dx.doi.org/10.1063/1.4927223
View Table of Contents: http://scitation.aip.org/content/aip/journal/chaos/25/7?ver=pdfcov
Published by the AIP Publishing

CHAOS **25**, 075410 (2015)

The joint space-time statistics of macroweather precipitation, space-time statistical factorization and macroweather models

S. Lovejoy[1,a)] and M. I. P. de Lima[2,3]
[1]*Physics Department, McGill University, Montreal, Quebec H3A 2T8, Canada*
[2]*Institute of Marine Research (IMAR) and Marine and Environmental Sciences Centre (MARE), Coimbra, Portugal*
[3]*Department of Civil Engineering, University of Coimbra, 3030-788 Coimbra, Portugal*

(Received 24 November 2014; accepted 9 July 2015; published online 31 July 2015)

Over the range of time scales from about 10 days to 30–100 years, in addition to the familiar weather and climate regimes, there is an intermediate "macroweather" regime characterized by negative temporal fluctuation exponents: implying that fluctuations tend to cancel each other out so that averages tend to converge. We show theoretically and numerically that macroweather precipitation can be modeled by a stochastic weather-climate model (the Climate Extended Fractionally Integrated Flux, model, CEFIF) first proposed for macroweather temperatures and we show numerically that a four parameter space-time CEFIF model can approximately reproduce eight or so empirical space-time exponents. In spite of this success, CEFIF is theoretically and numerically difficult to manage. We therefore propose a simplified stochastic model in which the temporal behavior is modeled as a fractional Gaussian noise but the spatial behaviour as a multifractal (climate) cascade: a spatial extension of the recently introduced ScaLIng Macroweather Model, SLIMM. Both the CEFIF and this spatial SLIMM model have a property often implicitly assumed by climatologists that climate statistics can be "homogenized" by normalizing them with the standard deviation of the anomalies. Physically, it means that the spatial macroweather variability corresponds to different climate zones that multiplicatively modulate the local, temporal statistics. This simplified macroweather model provides a framework for macroweather forecasting that exploits the system's long range memory and spatial correlations; for it, the forecasting problem has been solved. We test this factorization property and the model with the help of three centennial, global scale precipitation products that we analyze jointly in space and in time. © *2015 AIP Publishing LLC*. [http://dx.doi.org/10.1063/1.4927223]

Scaling analyses of precipitation and other atmospheric fields have shown the existence of an intermediate regime between the familiar weather and climate regimes: "macroweather," over the range of time scales from about 10 days to decadal, centennial scales. Although macroweather is important for seasonal, annual, and decadal forecasts, there have been no studies of its spatial variability and few studies of its temporal variability, with no coherent picture emerging. A recent paper (de Lima and Lovejoy, submitted) makes a step in this direction by systematically studying the separate temporal and spatial variabilities in three centennial, global scale precipitation products: one instrument based, one reanalysis based, and one satellite and gauge based. In this paper, we build on this work to analyze the joint space-time fluctuations using spectra as well as Haar structure functions allowing us to verify the prediction that the joint functions factor into separate spatial and temporal terms. We make explicit space-time stochastic models with roughly the observed statistics. Physically, factorization means that the spatial macroweather variability corresponds to different climate zones that multiplicatively modulate the local, temporal statistics. The findings provide a framework for macroweather models that can make forecasts exploiting the long range memory as well as the spatial correlations.

I. INTRODUCTION

Ever since at least (Van der Hoven, 1957) it has been recognized that the atmosphere undergoes a drastic transition in its statistical properties at time scales of the order of 2–10 days. At first, this was theorized as "migratory pressure systems of synoptic weather map scale…" and termed the "synoptic maximum" by Kolesnikov and Monin (1965) and Panofsky (1969); more recently, Vallis (2010) attributed it to baroclinic instabilities. However, following Lovejoy and Schertzer (1986), it was alternatively theorized as a transition scale τ_w between two scaling regimes at a scale corresponding to the lifetime of planetary sized structures. This interpretation was bolstered by the demonstration (Lovejoy and Schertzer, 2010c) that the scale can be theoretically estimated from first principles from knowledge of the solar output and the efficiency of conversion from solar to mechanical energy (≈4%). Further evidence in favor of the theory was the demonstration in Lovejoy and Schertzer (2013) that the spectrum of the ocean could be analogously explained (with a transition at ≈1 year). More recently, the theory successfully explained the statistical structure of the

---

[a)]Author to whom correspondence should be addressed. Electronic mail: lovejoy@physics.mcgill.ca.

Martian atmosphere (with a transition at about 1.8 days (Lovejoy *et al.*, 2014)). Physically, the transition time scale is the lifetime of planetary sized structures, fluctuations at shorter time scales are dominated by smaller structures with their corresponding shorter lifetimes. At longer time scales, there is a "dimensional transition," the spatial degrees of freedom rapidly become "quenched," the space-time statistics factorize into separate spatial and temporal functions (see below), at these time scales the statistics are those of several lifetimes of structures.

If we consider the temporal fluctuations in an atmospheric variable I over an interval Δt as $\Delta I(\Delta t)$, then in a scaling regime the mean fluctuations vary as $\langle \Delta I(\Delta t)\rangle \approx \Delta t^H$, where H is the fluctuation exponent (for Gaussian processes, it is equal to the Hurst exponent, "$\langle\ \rangle$" means statistical averaging). Lovejoy and Schertzer (2013) showed for rain as well as the thermodynamic and dynamical variables that the transition at τ_w was always between an $H > 0$ high frequency weather regime and an $H < 0$ low frequency "macroweather" regime. In particular, for rain, the transition scale τ_w varied somewhat with latitude from about 2–5 days, see Fig. 1(a) (a little less than for the temperature which is 5–10 days). The different behaviors ($H > 0$, $H < 0$) correspond to average fluctuations growing or decreasing with scale; in the macroweather regime, since $H < 0$, they tend to cancel so that averages over longer and longer times converge. However—at least for temperature, but probably also for the precipitation and other atmospheric fields—rather than converging to a fixed "climate" as one might expect, after about 10–30 years (industrial period) and ≈100 years (pre-industrial period), there is a transition to another scaling regime—the climate proper—again with fluctuations growing with scale ($H > 0$; see the rise in Fig. 1(a) beyond ≈30 years). In the pre-industrial period over the last millennia, the situation is not so clear since the macroweather-climate transition scale τ_c apparently has a great deal of spatial variability, see Lovejoy and Schertzer (2013), section 11.1.3.

Although the exact value of the preindustrial τ_c may still be uncertain, for the temperature field the basic three-scaling regime picture is relatively robust notably because (a) of the existence of high quality paleotemperature data that allow us to estimate the statistics at decadal and centennial scales for preindustrial epochs, (b) the temperatures are not too intermittent so that the uncertainties are smaller, (c) the theoretical and GCM modeling implications of anthropogenic effects on the temperature are much clearer than for precipitation, and (d) (deterministic) numerical models well reproduce the weather and macroweather regimes including exponents, as do (stochastic) turbulence based cascade models (see Sec. III).

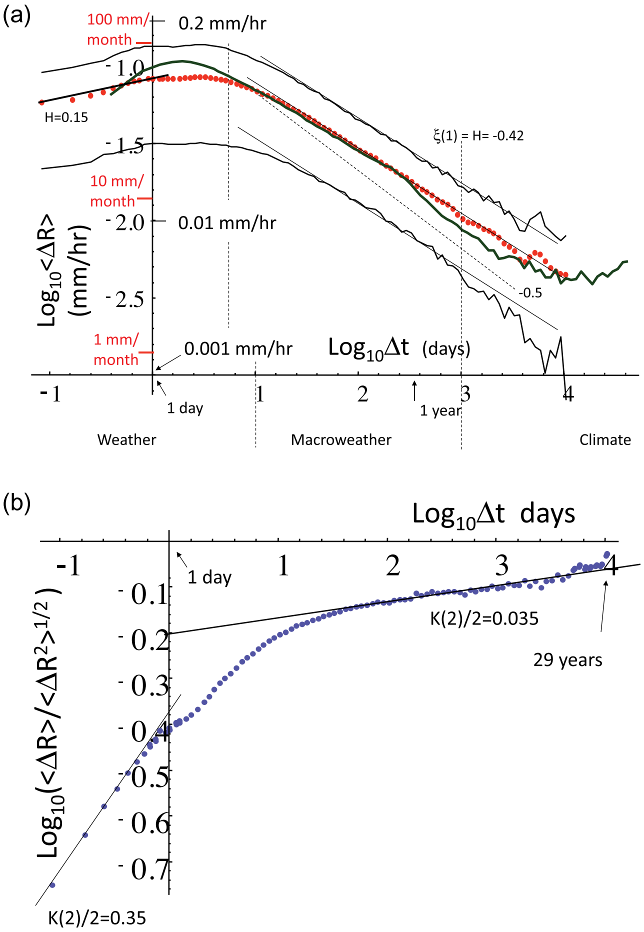

FIG. 1. (a) The first order structure function (the mean absolute Haar fluctuation) using precipitation data from the Climate Prediction Center (CPC, continental U.S.) gridded gauges (dots) as well as the corresponding structure function of the 20CR reanalysis at 45°N (6 h, 2° resolution, from 1871 to 2008, thick green line). $\langle \Delta R\rangle$ is the mean absolute fluctuation in the rain rate over a time interval Δt (i.e. $q = 1$). For the CPC product, we also show the corresponding grid point to grid point one-standard-deviation limits (thin) with reference lines slopes $H = -0.42$ (solid) and -0.5 (dashed, corresponding to a Gaussian white noise process). Also at the far left a reference line slope 0.15 indicates the weather regime H value (this value is sensitive to the treatment of low and zero rain rates, it is not too robust). NOAA's CPC product is unique in its high temporal resolution over a large number of contiguous grid points. The product analyzed was a (near complete) subset of the CPC data for the 29 years 1948–1976 (at this date there is a data gap of several weeks so that we did not extend the analysis to more recent times). The CPC data were gridded on $2.5° \times 2.0°$ boxes by using a modified Cressman Scheme (an interpolation technique); we used its central rectangular 13×21 point region from $-122.5°$ to $-72.5°$ longitude (every $2.5° \approx 210$ km at these latitudes), and from 30° to 54° latitude (every $2° \approx 220$ km). Each grid box had a near complete ≈257 000 hourly series. Haar fluctuations were used (see Section II B). Adapted with permission from Lovejoy *et al.*, Adv. Water Res. **45**, 37–50 (2012). Copyright 2012 Water Resources Research. (b)The ratio of the mean $q = 1$ and RMS fluctuations for the CPC dataset. Reference lines have slopes $K(2)/2 \approx C_1$ and show the transition from high intermittency behavior at scales less than a few days (the "weather regime") to low but not insignificant intermittency behavior at scales of months to years (the "macroweather regime"). Gaussian white noise would be flat ($K(2) = 0$). Reproduced with permission from Lovejoy *et al.*, Adv. Water Res. **45**, 37–50 (2012). Copyright 2012 Water Resources Research.

For precipitation, the basic picture seems to be the same, although there is more uncertainty. For example, in the weather regime, the existence of transitions from zero to finite rain rates breaks the scaling (Lovejoy *et al.*, 2008; de Montera *et al.*, 2009; Mandapaka *et al.*, 2010; Sun and Barros, 2010; Verrier *et al.*, 2010; Verrier *et al.*, 2011; Hoang *et al.*, 2012; and Gires *et al.*, 2013) but the distinction between real and spurious breaks due to instrumental problems at low rain rates is still under debate (see the review in Lovejoy and Schertzer (2013, section 4.4). In contrast, in the macroweather regime there are numerous papers showing scaling analyses with data spanning a range of weather and macroweather scales, but only a few that explicitly attempted to distinguish the two regimes and to estimate macroweather exponents (i.e., from several days to years or decades). Examples of the former include Douglas and Barros (2003), Pathirana *et al.* (2003), Bunde *et al.* (2005), Garcia-Marin *et al.* (2008), de Lima and de Lima (2009), Bunde *et al.* (2013), and Rysman *et al.* (2013); while examples of the latter are Ladoy *et al.* (1991), Tessier *et al.* (1996), de Lima (1998), Kantelhardt *et al.* (2006), and Lovejoy *et al.* (2012). The exponents from these studies are summarized in Table I of [de Lima and Lovejoy, submitted] (hereafter dLL) (see also Table 10.1 in Lovejoy and Schertzer (2013), they generally concur with the results discussed below—i.e., low intermittency and $H \approx -0.4$, Table I). It could be noted that while some of the papers cited in the former category did quote exponents in the macroweather regime, they suffered from technical issues that led to large inaccuracies: two types of relevant technical problems are discussed in Sec. III B.

Although the temporal statistics still need clarification, as far as we can tell, there have been no studies at all of spatial macroweather statistics. This is partly due to the diversity of analysis techniques used and partly due to the strong focus on scaling statistics from individual stations. We need clarification of (a) the (possible) variation of the exponents with latitude, (b) their variation over land, over ocean, (c) the global scale averaged values, (d) the expected anthropogenic (low frequency) effects, (e) the degree of agreement/disagreement between different techniques for estimating areal precipitation, and (f) the joint space-time macroweather statistics. Issues (a)–(e) were addressed in dLL; while the joint space-time statistics needed for macroweather modeling with the related theoretical and modeling issues are the focus of this paper.

Empirical investigations cannot be divorced from theoretical frameworks and macroweather precipitation is no exception. Lovejoy and Schertzer (2010c) and Lovejoy and Schertzer (2013) showed that space-time turbulent cascade models (the Fractionally Integrated Flux, FIF model) which were developed for weather scales could be extended to the macroweather regime by the simple expedient of allowing the cascades to develop starting from an (outer) time scale much longer than τ_w (the Extended FIF (EFIF) model). The argument—summarized in more detail in Sec. III—leads to the conclusion that space-time macroweather statistics should—at least approximately—satisfy a fundamental space-time statistical factorization property. For example, applied to the spectral density $P_{xyt}(k_x,k_y,\omega)$ in horizontal space-time (x,y,t) (k_x, k_y, ω are the corresponding nondimensional wavenumbers and frequency), it implies that $P_{xyt}(k_x,k_y,\omega) = P_{xy}(k_x,k_y)P_t(\omega)$, where $P_{xy}(k_x,k_y)$ and $P_t(\omega)$ are the horizontal and temporal spectral densities, respectively. This contrasts with the space-time weather statistics that have spectra involving (turbulent) space-time scale functions such as $(k_x^2 + k_y^2 + \omega^2)^{1/2}$ raised to various powers and that therefore cannot be factored in this way [see Pinel *et al.* (2014) for extensions to cases with mean advection, and Pinel and Lovejoy (2014) for further generalizations to waves). Although it was not explicitly theoretically proposed until Lovejoy and Schertzer (2013), factorization means that different (spatially distributed) climate zones modulate the local temporal statistics without changing their type (e.g., their temporal scaling). The factorization principle is already implicitly used in practical climatology when, for example, local station statistics are nondimensionalized by local standard deviations or by using (nondimensional) probability distributions so as to "homogenize" the data or to produce various climate indices that may be compared between different stations with different climates.

II. DATA AND FLUCTUATIONS

A. The data

We are interested here in the space-time structure of precipitation over time scales from about 1 month to centuries (and longer if possible), and in space from global scales to scales of a few degrees (or smaller if possible). The main relevant gauge based dataset is the Global Historical Climatology Network product (GHCN; Lawrimore *et al.*, 2011) available from the NOAA site, which is monthly data for the period 1900–2012 at 5° × 5° resolution. In order to alleviate issues to do with missing data, series consistency, etc., only the precipitation anomalies were reported (i.e., with the annual cycle removed and relative to the 1961–1990 reference period). The data are gauge based, they are therefore restricted to land (but virtually all the pixels have significant outages). By excluding the oceans, the GHCN product will likely give a biased view of global scale precipitation. This is true not only because the oceans comprise 70% of the earth's surface but also because oceanic precipitation is likely to be different from precipitation over land, and this includes a potentially much stronger response to anthropogenic warming. The only two relevant ocean precipitation

TABLE I. Macroweather precipitation anomaly and raw fluctuation exponents (H). The exponents were generally not estimated with high accuracy partly because of the high intermittency (the scaling was noisy) but also because more precise values are not warranted since the exact limits of the scaling ranges are not clear. Note that while the data agree quite well on the temporal exponent, they disagree strongly on the spatial exponent including the sign (the EW and NS values of H were judged to be quite close so only a single spatial value was given). For the spatial 20CR and Smith fields (where the absolute precipitation rates were known, not just the anomalies), the spatial H's for the raw and anomaly fields were quite close (except at the larger distances/angles, 4th column, where the anomalies seem close to the GHCN anomalies). CPC refers to the Climate Prediction Center, GHCN the Global Historical Climate Network, 20CR the Twentieth Century Reanalysis, and "Smith" refers to Smith *et al.* (2012) IR satellite data based product.

	Time	Space anomaly (angle subtended <50°–80°)	Space anomaly (angle subtended >50°–80°)	Space raw data
CPC	−0.42	…	…	…
GHCN	−0.4	−0.2	−0.2	…
20CR	−0.4	0.2	−0.2	0.2
Smith	−0.4	0.1	−0.2	0.15

datasets of which we are aware from the Twentieth Century Reanalysis (20CR; Compo *et al.*, 2011) and the Smith *et al.* (2008; 2012) satellite/gauge reconstruction (hereafter abbreviated "Smith"). Both of these datasets are very indirect, for example, the 20CR data (which is available at 2° × 2° and 6 h resolution, much higher than needed here) are derived solely from surface pressure data and monthly Sea Surface Temperature (SST) data, the precipitation is entirely inferred from a numerical model; the result—a "reanalysis"—is a kind of data/model hybrid (the product used here is monthly at 1.875° resolution, see, e.g., Kalnay (2003) for the data assimilation techniques used to produce reanalyses). In comparison, the Smith data use a gauge calibrated Infra Red satellite rain algorithm to infer global scale rain over the satellite observation period (1979–2012). This is then used to calculate Empirical Orthogonal Functions (EOF's). Finally, in the pre-satellite era, the historic land based gauge data (GHCN) are used to estimate the coefficients of each EOF, yielding global scale estimates at 5° × 5°, monthly resolution. dLL discusses, compares, and contrasts these datasets' details as functions of space and time scale. For the means of the absolute rates for the Smith and 20CR data (the GHCN gives only anomalies), they find that there is a disagreement of ≈20% for the mean land precipitation estimates, but only about 5% for the ocean estimates: overall the disagreement is by about 10% for the global values.

B. Quantifying the variability over scales: Fluctuations, structure functions

Consider the global scale averages, the anomalies are shown in Fig. 2(a) (a typical space-time plot is shown in Fig. 2(b)). Notice that the gauge based product (GHCN) is much more variable (more high frequencies are present) than the Smith product, itself more variable than the 20CR product. We can also note that while there is some overall agreement at the lowest frequencies, the higher frequencies are often in disagreement. In order to quantify the high and low frequency variability, we can consider the mean and the root mean square (RMS) fluctuations.

While many fluctuation definitions are possible, in this paper we use Haar fluctuations. The Haar fluctuation of the precipitation $\Delta R(\Delta t)$ at time scale Δt is simply the difference of the mean of R over the first and second halves of the interval Δt

$$(\Delta R(\Delta t))_{Haar} = \frac{2}{\Delta t}\int_{t-\Delta t/2}^{t} R(t')dt' - \frac{2}{\Delta t}\int_{t-\Delta t}^{t-\Delta t/2} R(t')dt', \quad (1)$$

where we have added the subscript "Haar" to distinguish it from other common definitions of fluctuation and we have suppressed the t dependence because we will assume that the fluctuations are statistically stationary. Haar fluctuations are simple to understand because with an appropriate "calibration" constant (a factor 2 used throughout this paper), in scale regions where $H > 0$, the Haar fluctuations are nearly equal to the differences ("dif"), in scale regions where $H < 0$, they are nearly equal to the anomalies ("anom")

$$(\Delta R(\Delta t))_{dif} = R(t+\Delta t) - R(t),$$
$$(\Delta R(\Delta t))_{anom} = \frac{1}{\Delta t}\int_{t}^{t+\Delta t} R'(t')dt'; \quad R' = R - \bar{R}, \quad (2)$$

where $\bar{R}$ is the mean over the entire series. Mathematically, we have $(\Delta R(\Delta t))_{Haar} \approx (\Delta R(\Delta t))_{dif}$, $0 < H < 1$, and $(\Delta R(\Delta t))_{Haar} \approx (\Delta R(\Delta t))_{anom}$, $-1 < H < 0$.

Now that we have defined the fluctuations, we need to characterize them; the simplest way is through (generalized) structure functions (generalized to fluctuations other than the usual differences, and generalized to moments q of order other than the usual value 2): $\langle \Delta R(\Delta t)^q \rangle$, where "$\langle . \rangle$" indicates statistical (ensemble) averaging.

Physically, if the system is scaling, then the fluctuations are related to the driving flux φ by

$$\Delta R(\Delta t) = \varphi_{\Delta t}\Delta t^{H}, \quad (3)$$

where we have used the subscript "Δt" on φ to indicate that it is the flux averaged at resolution Δt. The qth order structure function is

$$\langle \Delta R(\Delta t)^q \rangle = \langle \varphi_{\Delta t}^{q} \rangle \Delta t^{qH}. \quad (4)$$

Turbulent fluxes are conserved from scale to scale so that $\langle \varphi_{\Delta t} \rangle =$ constant (independent of scale) implying that $\langle \Delta R \rangle \propto \Delta t^{H}$, so that H is the mean fluctuation exponent. Beyond the simplicity of interpretation, the Haar fluctuations give a good characterization of the variability for stochastic processes with H over the range $-1 < H < 1$ which includes all the common geophysical series and processes. In contrast, fluctuations defined as differences or as anomalies are only valid over the narrower ranges of $0 < H < 1$, $-1 < H < 0$, respectively (see Lovejoy and Schertzer (2012b) and Lovejoy *et al.* (2013)). Outside these ranges in H, the fluctuation at scale Δt is no longer dominated by frequencies $\approx \Delta t^{-1}$ so that the fluctuations depend spuriously on details of the finite data sample, specifically either the highest or the lowest frequencies that happen to be present.

The generic scaling process is a multifractal process so that, in general, φ has statistics

$$\langle \varphi_{\Delta t}^{q} \rangle \approx \Delta t^{-K(q)}, \quad (5)$$

where $K(q)$ is a convex function. Substituting this into Eq. (4), we obtain

$$\langle \Delta R(\Delta t)^q \rangle \approx \Delta t^{\xi(q)}; \quad \xi(q) = qH - K(q), \quad (6)$$

where $\xi(q)$ is the "structure function exponent." Although we return to this in more detail in Sec. III, for the moment note that the mean ($q = 1$) flux $\langle \varphi_{\Delta t} \rangle$ is independent of Δt, so that $K(1) = 0$ and hence $\xi(1) = H$. Note also that for quasi Gaussian processes, none of the moments of $\varphi_{\Delta t}$ have any scale dependence so that $K(q) = 0$ and $\xi(q) = qH$ (all the scale dependence is characterized by H). A useful characterization of $K(q)$ is provided by $C_1 = K'(1)$ which quantifies the intermittency near the mean ($q = 1$, see below). Finally, the RMS fluctuation $\langle \Delta R(\Delta t)^2 \rangle^{1/2}$ has exponent $\xi(2)/2$ so

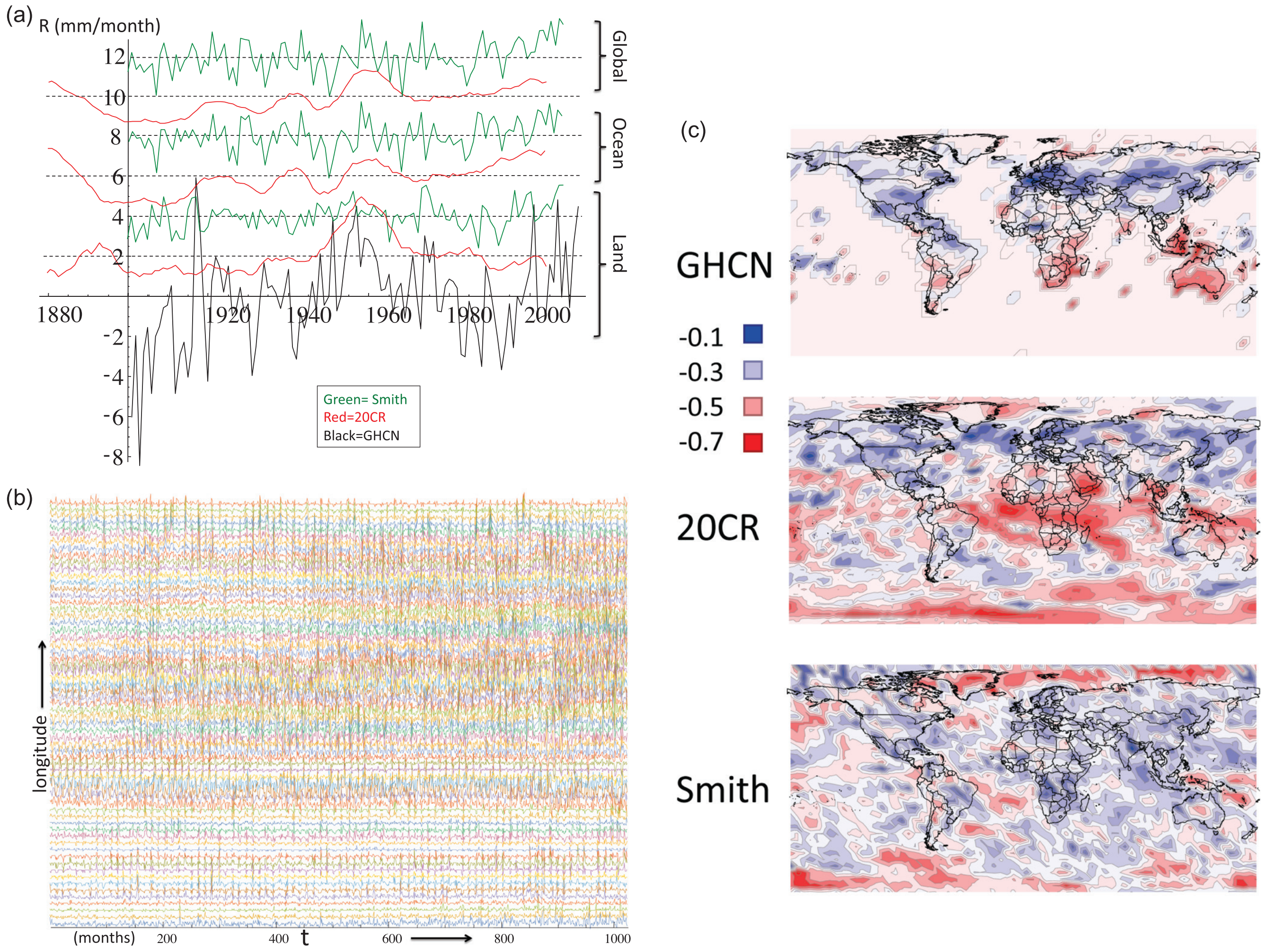

FIG. 2. (a) The annual precipitation rate anomalies averaged over land only (bottom), ocean (middle), and globally (top). The black (thick) curve is the Global Historical Precipitation network (GHCN) from January 1900 to December 2012. The red (dashed) curves were the 20CR from 1880 to 2004 and the green (thin) curves were for the Smith product. The GHCN and Smith *et al.* (2012) (Smith) products were at 5° × 5° resolution, the 20CR data were at 1.875° resolution. For clarity, the data were shifted upwards by 2 mm/month increments as indicated by the dashed horizontal lines. (b) The 20CR anomaly data at 33°N, 1024 months (starting in 1871), 64 consecutive longitudes at 1.875° resolution starting from 0° and moving to the west. This illustrates the space-time macroweather structure that is modeled below; compare this with the models in Figs. 6(a)–6(c). (c) The pixel scale world maps of the distribution of H_t for monthly precipitation for the three datasets discussed in the paper (5° × 5°, 3.75° × 3.75°, and 5° × 5° resolutions for GHCN, 20CR, and Smith datasets, respectively, from top to bottom; the 20CR resolution was degraded 2 × 2 pixels so as to be more comparable to the resolutions of the other datasets). The transition from reddish to bluish occurs at roughly the mean H_t value of -0.4. The exponents were estimated from the annually detrended data using the Haar analysis technique with exponents fit over the range of 6 months to 12 years (to avoid possible biases at low frequencies due to anthropogenic effects or poor statistics). The pink in the GHCN map corresponds to no data (mostly oceans).

that the error in using the quasi-Gaussian approximation to estimate H (i.e., the approximation $\xi(2)/2 = H$) is $\xi(2)/2 - H = K(2)/2$. In the temporal macroweather domain, the latter is typically small—in the range of 0.02–0.04 so that the approximation $\xi(2)/2 \approx H$ is fairly accurate. Figure 1(b) shows a direct estimate using the enormous CPC hourly gridded raingauge product over the continental U.S. ($\approx 7 \times 10^7$ gridded quantities were used in the analysis, a product already derived from a much larger set of station series measurements). We see that the temporal intermittency as quantified by $K(2)/2$ is large at weather scales (lower left part of the figure, $K(2)/2 \approx 0.35$) but is much smaller at macroweather scales (≈ 0.035, upper right part of the figure). The use of the second moment is conventional since it directly determines the exponent β of the spectrum $E(\omega) \approx \omega^{-\beta}$, where ω is the frequency: $\beta = 1 + \xi(2)$; we therefore have used the RMS statistics below. However, in dLL and in Section III B (using a different method) we show that spatial macroweather has $K(2)/2 \approx 0.1$, so that in the spatial domain the approximation $\xi(2)/2 \approx H$ is poor, and a full multifractal characterization is needed (i.e., including $K(q)$). Note that in the higher frequency weather regime, the spatial intermittency is even stronger: $K(2)/2 \approx 0.4$ (see Tables I and II for global scale weather regime estimates). Finally, even when $K(2)/2$ is small, the probability distribution of the fluctuations may be far from Gaussian, indeed power law probability tails are a generic consequence of the space-time scaling. For example, dLL shows the distribution of monthly precipitation rate changes $Pr(\Delta R > s) \approx s^{-q_D}$ with $q_D = 3.6$ (a bit lower than the macroweather temperature value $q_D \approx 5$ but close to the weather scale precipitation value $q_D \approx 3$, see Table 5.1b in Lovejoy and Schertzer (2013) for a review with over a dozen references with $q_D \approx 3$).

TABLE II. A comparison of the spatial intermittency parameter C_1 and the effective outer scale (L_{eff}) for various data products at weather scales (ECMWF: 3 h resolution; 20CR: 6 h resolution; CPC: 1 h resolution; TRMM: 4 days resolution) and at macroweather scales (all at one month). ECMWF refers to the European Centre for Medium range Weather Forecasting interim reanalysis. The weather analyses and parameters were taken from Lovejoy *et al.* (2012). The "time" column refers to pixel scale spatial resolutions. For the macroweather regime, the C_1 values of the globally averaged series were slightly higher. Also, the CPC data in the macroweather regime give $C_1 = 0.04$ (see Fig. 1(b)). The macroweather intermittencies (C_1) are significantly lower than the corresponding weather values, especially in time. The macroweather 20CR row reports two zonal (EW) values from Figs. 4(c) and 4(d) corresponding to latitudes 30°–60° N and 0°–30° N. The exponents of the spatial anomalies are given in the table.

	C_1			L_{eff} (km)	
Product	Time	EW	NS	EW	NS
			Weather		
ECMWF	0.34	0.41	0.45	50 000	32 000
20CR	0.21	0.26	…	25 000	…
CPC	0.37	0.49	0.51	40 000	32 000
TRMM	0.30	0.27	0.32	40 000	16 000
			Macroweather		
GHCN	0.01	0.11	…	…	…
20CR	0.02	0.09–0.12	0.19	30 000–55 000	27 000
Smith	0.01	0.15	0.21	25 000	10 000

C. Overview of temporal and spatial macroweather precipitation statistics

In dLL, the GHCN, 20CR, and Smith datasets were systematically analyzed and compared over the range of 1 month to ≈100 years and from one pixel (primarily 5° × 5°) to global scales; the overall summary of the statistical properties is shown in Tables I and II. In the time domain, for all products, we found very similar behaviors: for land, ocean, global, and for various latitude bands for pixel and global scales, we found $H \approx -0.4$ which is a little higher than Gaussian white noise ($H = -\frac{1}{2}$), the main differences being the amplitudes of the fluctuations (e.g., the RMS variability at a given scale such as one year) and the outer scale τ_c, the transition scale to the climate regime (here presumably associated with anthropogenic effects). The global scale analyses had $\tau_c \approx 20$ years, whereas the pixel scale analyses (including several individual long station series from Portugal) had $\tau_c \approx 40$ years. Here and below, when needed to avoid confusion, we introduce the subscripts "*t*" for temporal and "*x*" for spatial exponents.

Analyzing the time series on a pixel by pixel basis (see Fig. 2(c)), we found: $H_t \approx -0.41 \pm 0.07$, -0.38 ± 0.09, and -0.43 ± 0.10 for the GHCN, 20CR, and Smith data, respectively (the corresponding estimates of the intermittency parameter C_1 were 0.026 ± 0.02, 0.020 ± 0.025, and 0.00 ± 0.01, the uncertainties here and above indicate one standard deviations of the dispersion of the values about the mean). H_t is thus roughly globally constant with a value ≈−0.4. In order to see if the spread is simply due to estimation errors, in Fig. 2(c) we show the spatial distribution of H_t estimates. There is some spatial organization and reasonable agreement between the GHCN and 20CR maps, less agreement with the Smith map. There is also a tendency for H_t to be low over oceans (especially the Pacific), this is physically plausible since H_t values closer to zero correspond to longer range predictability (Lovejoy *et al.*, in press). However, the values should be taken with caution since the 20CR temperatures have lower H over the oceans and the 20CR estimates the precipitation rather indirectly.

Since C_1 is very small, H_t alone characterizes the long range statistical dependencies in the macroweather precipitation process and it turns out that the effective "memory" depends sensitively on H_t: the white noise value −1/2 corresponds to no memory (no predictability) while the value $H_t = 0$ to an infinite memory (perfect predictability), see Lovejoy *et al.* (in press). One way to quantify the memory is the fraction of the variance that can be explained by forecasting one time step into the future by using the past data (i.e., a one month forecast with monthly data, a one year forecast with yearly data). For the global temperature, $H_t \approx -0.2$ and about 35% of the variance can be explained, for ocean temperatures (SST's) $H_t \approx -0.1$ and 65% can be explained. In contrast, for precipitation, with $H_t \approx -0.4$ only 4% can be explained (this might still be useful, especially if the skill could be increased with the help of co-correlates). For the temperature field, H_t is found to vary relatively systematically, in particular, being strongly correlated with land or ocean location with the lower (more predictable) H_t's generally over the ocean. The rough agreement on the geographical distribution of H_t values in Fig. 2(c) is therefore important.

The rough agreement between different datasets on temporal scaling exponents is consistent with macroweather precipitation being reasonably estimated, and this in spite of the quite different techniques used to estimate precipitation rates (instruments, reanalyses, and satellite based). While such an agreement is a necessary condition for the products to agree with each other, it is not sufficient: indeed, each product could be from a statistically independent realization of the same stochastic process. To gain further confidence in the quality, accuracy of the precipitation products, dLL therefore compared the product fields directly to each other by considering the difference between pairs of the three products and studied the fluctuation statistics of the resulting difference fields.

The dLL analysis showed that the agreement between the products was not so good. For example, for the GHCN and 20CR products, the agreement at scales below a year but also greater than 10 years was low. Similarly, for the global scale 20CR and Smith products (the two that were not missing data), there was poor agreement until scales of 5 years or so and poor agreement for monthly data at scales beyond about 30 years (significant for anthropogenic effects).

In space, the situation was somewhat different with poor agreement for scales below about 20°–30° latitude. It also seemed that the spatial scaling exponents were significantly different, with the 20CR and Smith products being much smoother (the Smith and 20CR, H_x were about 0.3 larger than for the GHCN product, although at the very largest scales they were close, see Table I). The smoothness may be an artefact of the limitations of the 20CR model and the smoothness of the satellite IR fields that were used to infer the Smith product.

The spatial and temporal scaling properties of macroweather precipitation that we have just described are qualitatively very similar to those of macroweather temperatures as analyzed, for example, in Lovejoy and Schertzer (2012a; 2013). The main differences between temperature and precipitation statistics are that the latter have generally lower temporal H values, higher spatial C_1 values, and somewhat longer transition scales τ_c. Similar comments also pertain when comparing weather scale temperatures and precipitation (although in the weather regime, the intermittency parameter C_1 is much larger for precipitation than for temperature). This indicates that precipitation may be treated in the same theoretical framework as the temperature (and other atmospheric fields) which can be modeled with the help of space-time cascade processes. In this picture, the scaling laws are emergent high level statistical (turbulent) laws expected to apply in the limit of high nonlinearity.

III. MACROWEATHER MODELS AND SPACE-TIME STATISTICAL FACTORIZATION

A. Theoretical considerations

dLL and the other studies cited above indicate that in the macroweather regime there is good scaling in space and in time. This basically reflects the absence of strong scale breaking processes. Scaling symmetries also hold with high accuracy in the weather regime; Lovejoy and Schertzer (2013) is a review for 30 years of research supporting this conclusion; however, the single Fig. 3 is enough to show—at least for thermal infra red satellite data (the type used by the Smith algorithm to infer precipitation)—that the scaling symmetry is in fact quite exact. The figure uses nearly 1300 h of hourly geostationary MTSAT data (at 30 km resolution) from a 8000 × 13 000 km^2 region centred on the equatorial Pacific (see Pinel *et al.* (2014) for details). It can be seen that the zonal (i.e., EW), meridional (NS), and temporal spectra are nearly identical up to ≈(5–10 days)$^{-1}$ and are nearly perfect power laws (most of the deviations from linearity in the figure can be accounted for by the finite resolution and finite data "window," see the black line that theoretically takes these limitations into account). The main exceptions are the two small spectral "bumps" at (1 day)$^{-1}$ and (12 hours)$^{-1}$, both due to the diurnal cycle. These 1-D spectral densities were obtained by successively integrating out the complementary variables in the full (horizontal) space-time spectral density $P_{xyt}(k_x,k_y,\omega)$. This figure—and many others in Pinel *et al.* (2014)—show that the spectrum satisfies the isotropic scaling symmetry

$$P_{xyt}(\lambda k_x,\lambda k_y,\lambda\omega)=\lambda^{-s}P_{xyt}(k_x,k_y,\omega), \tag{7}$$

where empirically, $s=\beta+2\approx 3.4$ (note that at any given scale P_{xyt} displays anisotropy; Eq. (7) simply implies that the anisotropy does not change with scale, see Pinel *et al.* (2014) for the full analysis), and see Pinel and Lovejoy (2014) for the interpretation of spectra in terms of waves and turbulence. This result applies in the Euclidean frame; in the Lagrangian (co-moving) frame, the space-time relation is no longer isotropic, the lifetime τ of a structure size l is $\tau=\varepsilon^{-1/3}l^{2/3}$, where ε is the turbulent energy flux.

By necessity, the scale symmetry (Eq. (7)) can only hold up to planetary scales (L_w); this implies a breakdown in the time domain at scales τ_w which is interpreted as the lifetime of planetary scale structures. In Fig. 3, the breakdown occurs when the colored lines diverge from the black line which represents perfect scaling but with deviations due to the finite accessible region of Fourier space (rectangular with square pixels). We find a breakdown at $k\approx(5000\,\mathrm{km})^{-1}$ and $\omega\approx(5\,\mathrm{days})^{-1}$; Lovejoy and Schertzer (2010c) describes how this is determined by the turbulent energy flux ε (power/mass): $\tau_w=\varepsilon^{-1/3}L_w^{2/3}$, where L_w and τ_w are the outer space and time scales of the weather regime and ε itself is determined by the solar flux. This theory well describes the spectrum of many of the atmospheric variables, ocean temperatures, as well as the Martian weather and macroweather (Lovejoy *et al.*, 2014).

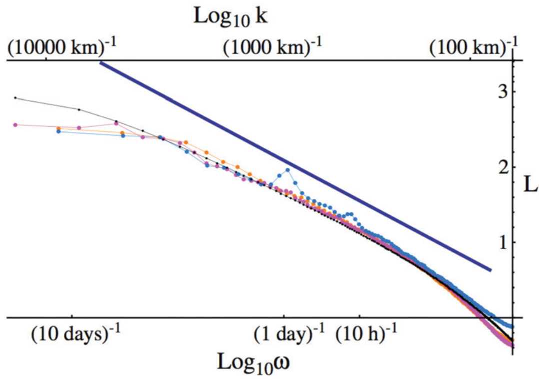

FIG. 3. 1D spectra of MTSAT thermal IR radiances; the Smith product was developed with very similar IR satellite radiance fields. In black: the theoretical spectrum using parameters estimated by regression from Eq. (7) and taking into account the finite space–time sampling volume. The one dimensional spectra are $E_x(k_x)\approx k_x^{-\beta x}$, $E_y(k_y)\approx k_y^{-\beta y}$, and $E_t(\omega)\approx\omega^{-\beta t}$ with $\beta_x\approx\beta_y\approx\beta_t\approx 1.4\pm 0.1$; $s\approx 3.4\pm 0.1$. The straight line is a reference line with slope -1.5 (blue). Pink: zonal spectrum; orange: the meridional spectrum; blue (with the diurnal spike and harmonic prominent): temporal spectrum. Reproduced with permission from Pinel, J. and Lovejoy, S., Atmos. Chem. Phys. **14**, 3195–3210 (2014). Copyright 2014 European Geosciences Union.

B. Spatial intermittency, multifractality, cascades

We have mentioned that the spatial intermittency is much stronger than the temporal intermittency. One way to demonstrate this is to use the Haar fluctuations directly, estimating $\xi(q)$ from the exponents of the qth order moments and then to estimate $K(q)$ as $-\xi(q)+q\xi(1)$ (see Eq. (6)). Due to the missing data, this was the approach followed for the GHCN data (see Tables I and II). However, for the 20CR and Smith data, we can easily estimate φ and hence $K(q)$ directly; for example, using Eq. (3) we can readily obtain

$$\frac{\varphi}{\langle\varphi\rangle}=\frac{\Delta R}{\langle\Delta R\rangle}. \tag{8}$$

If ΔR is estimated at the smallest available scale—for these complete, gridded data, we used the absolute second finite difference along the transect—then Eq. (8) shows that the normalized high resolution flux is obtained by dividing by the mean fluctuation $\langle\Delta R\rangle$. This high resolution flux can then be systematically degraded to lower resolution by averaging. The generic multifractal process is a multiplicative cascade; if such a process starts at outer scale L_{eff}, then the statistics follow:

$$\langle\varphi_{\lambda'}^{q}\rangle=\lambda'^{K(q)};\quad \lambda'=L_{eff}/\Delta r\,, \tag{9}$$

where λ' is the scale ratio of the outer scale to the resolution scale Δr of the degraded flux (see Eq. (5)). In empirical analyses, L_{eff} is not known *a priori*, it has to be estimated from the data; here we use a convenient scale ratio based on $L_w = 20\,000$ km, which is the largest distance on the earth (half a circumference), i.e., $\lambda = L_w/\Delta r$. If Eq. (9) holds, then, for all q the lines of $\log \langle \varphi_\lambda^q \rangle$ against $\log \lambda$ will cross at a scale corresponding to $\lambda_{eff} = L_w/L_{eff}$.

We mentioned in the introduction that there are two technical issues that have not always been carefully considered and which have led to incorrect macroweather exponent estimates; they both involve incorrect flux estimates. For example, if daily precipitation is analyzed by estimating the flux as indicated (Eq. (8); by absolute first or second differences for ΔR), then one will obtain correct trace moment estimates of the weather regime exponents. However, the scaling (and exponents) of these daily resolution fluxes in the macroweather regime (e.g., when daily fluxes are averaged to monthly values), will be different from the scaling and exponents that would be obtained if we first took monthly averages and then estimated the flux from the absolute differences of monthly resolution averages before degrading the resolution further. It is the latter method that gives the correct macroweather exponent estimates. The mathematical reason for the difference is that taking *absolute* differences at the finest resolution (Eq. (8)) is a nonlinear transformation: the physical reason is that the weather and macroweather fluxes are physically different. Alternatively, if one has monthly data but one neglects to take the absolute differences before degrading (i.e., implicitly assuming that the rain rate is already a pure cascade with $H = 0$), then one has $\xi(q) = -K(q)$ (Eq. (6) with $H = 0$ instead of ≈ -0.4), so that one can easily find the values, $C_1 \approx 0.6$ (with H implicitly $= 0$) instead of the correct values $H \approx -0.4$, $C_1 \approx 0$ (e.g., they give the same $\xi(2)$, hence the same spectral exponent, see Eq. (10) below with $\alpha \approx 0.6$).

Figures 4(a) and 4(b) show the trace moment result when the various moments of order $2 \geq q \geq 0$ are estimated for the Smith anomaly data (i.e., the difference between the raw precipitation data and the long term averages, see Sec. III D) in the zonal and meridional directions, respectively (even if the intermittency is low, higher order moments may diverge hence it is best to use only these relatively low order moments). It can be seen from the log-log linearity that the scaling is excellent up to about $10\,000$ km (it is a little better in the zonal direction). In addition, the lines plausibly cross at a scale of the order of the size of the planet (see Table II); the fact that L_{eff} can be a little larger than the size of the earth (L_w) is because, even at planetary scales (20 000 km), there is some residual variability due to the interaction of the precipitation field with other atmospheric fields: L_{eff} is simply the "effective" scale at which the cascade would have had to start in order to explain the statistics over the observed range. Figures 4(c) and 4(d) show similar analyses for the 20CR anomaly data and 4(e) and 4(f) show the trace moments of the long term averages. This shows some differences between anomalies and long term averages with larger outer scales (meaning more variability at any given scale), but with no clear trends for C_1 (i.e., the rate at which the variability near the mean changes with scale).

The slopes in Fig. 4 determine $K(q)$ (Eq. (9)); the latter is a convex function, equivalent to an infinite number of parameters. Fortunately, one can avail of a multiplicative analogue of the usual (additive) central limit theorem for random variables (the climate process, see below). This shows that under fairly general circumstances $K(q)$ is determined by only two parameters that define multifractal "universality classes"

$$K(q) = \frac{C_1}{\alpha - 1}(q^\alpha - q); \quad 0 \leq \alpha \leq 2, \tag{10}$$

where α is the Levy index and C_1 is the codimension of the mean (Schertzer and Lovejoy, 1987). From Eq. (10), we see that $C_1 = K'(1)$; this provides a convenient way of estimating the parameters (for α, one can use $\alpha = K''(1)/K'(1)$). Table II (bottom rows) shows the resulting parameter estimates for the macroweather regime and compares these with those in the weather regime (top rows). For the Smith data, the estimates of the parameter α were all in the range of 1.7–1.85 (see also Table III for the 20CR that were a bit more dispersed). Also, note that the difference between the exponents of the RMS and mean (important for interpreting the slopes in the RMS Haar graphs), $\xi(2)/2 - H = K(2)/2 = A_\alpha C_1$, where $A_\alpha = (2^\alpha - 1)/(\alpha - 1)$. For example, if we take $1.85 > \alpha > 1.7$ we find $0.95 > A_\alpha > 0.9$ (near one), so that C_1 provides a good estimate of the error in using the RMS exponent $\xi(2)/2$ in place of H. From Table II, we see that, in space, the difference $\xi(2)/2$–H can be readily in the range of 0.1–0.2: it is significant. Also notable in Table II is the comparison of weather and macroweather exponents and outer scales. We can see that while the outer scales are very similar, weather scale precipitation is much more variable (the C_1 parameter is much higher) than macroweather precipitation.

C. Space-time cascades, the FIF and EFIF models, and macroweather factorization

The generic multiplicative cascade process φ with multifractal statistics (Eq. (9)) can be modelled either by direct multiplication of "multiplicative increments" discretized on a dyadic tree (i.e., with large "parent" structures multiplied by reduced scale "daughter" structures) or, equivalently, produced by exponentiating an additive generator Γ, the latter method having the advantage of being continuous in scale (rather than repeating only with integer powers of an integer scale ratio as in the "discrete in scale" dyadic cascades), see Subsection 1 of the Appendix for a review. However, most processes of interest are not the direct result of a cascade process, the prototypical example being the velocity field in Kolmogorov turbulence. In this case, velocity fluctuations scale as $\Delta v \approx \varepsilon^{1/3} \Delta x^H$, where ε is the energy flux (from large to small scales) and $H = 1/3$. In the Fractionally Integrated Flux (FIF) model, velocity fields with the corresponding H are obtained by fractionally integrating the flux (in this case $\varepsilon^{1/3}$). A fractional integration is the most general linear transformation, if it is of order H, it is simply a power law filter, e.g., $|\underline{k}|^{-H}$ where k is a wavenumber. In real space dimension d, it is a convolution with the singularity $|\underline{r}|^{-(d-H)}$ (we have

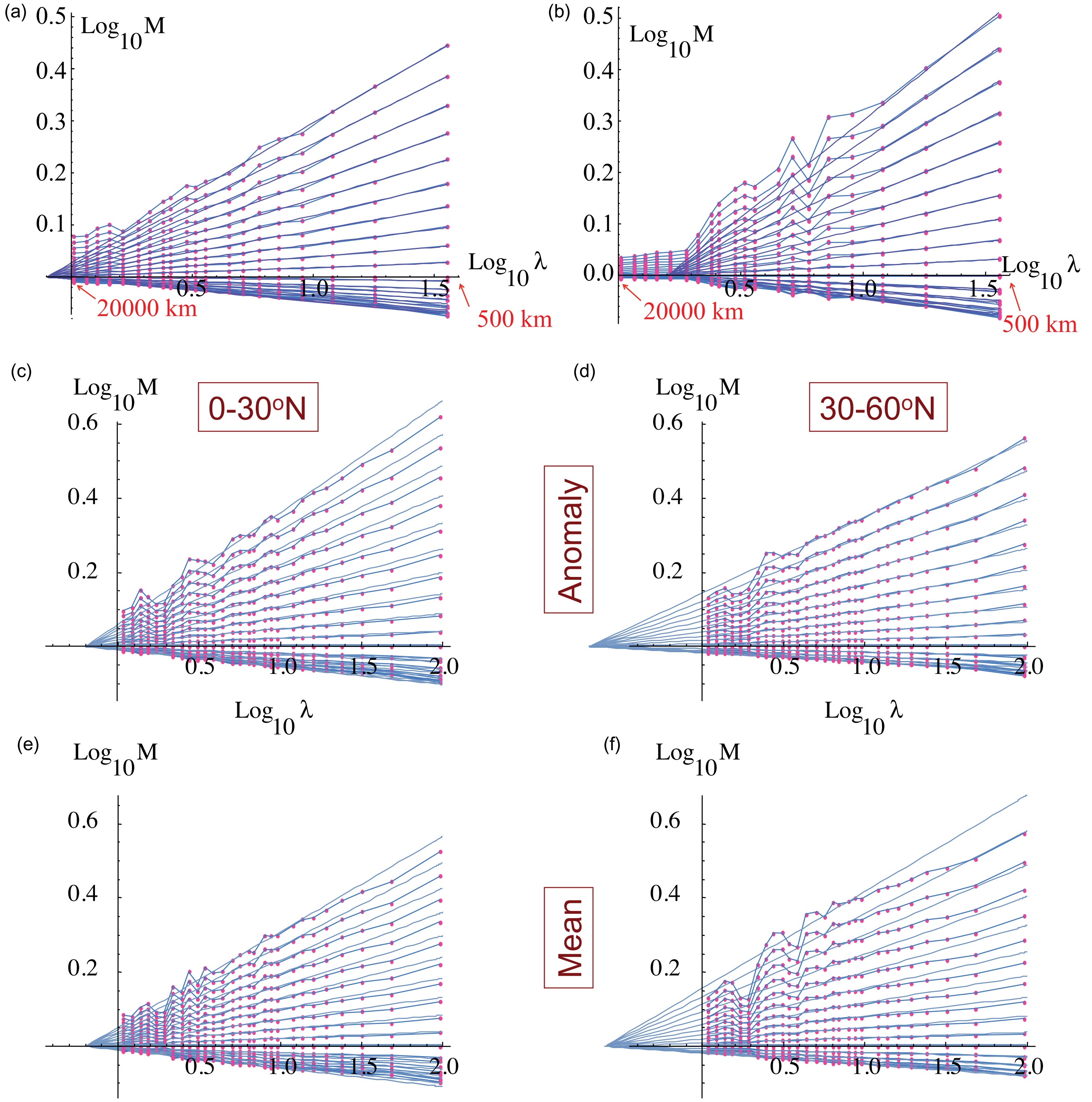

FIG. 4. (a) Zonal (EW) trace moments for the Smith anomaly data spanning the region from −45° to 45° latitude, $M = \langle \varphi_\lambda^q \rangle$. Note the convergence close to 20 000 km and the low C_1 value. $L = L_w/\Delta r$ with $L_w = 20\,000$ km. The top curve is for $q = 2$, with q ranging down to 0.1. (b) Same as (a) but for the meridional (NS) direction. (c), (d), (e), and (f): The trace moment analyses (with $M = \langle \varphi_\lambda^q \rangle$) of the 20CR anomalies in the east-west direction (at 1.875° resolution), averaging the data over the bands from the equator to 30°N ((c) and (d)) and from 30°–60°N ((d) and (f)). The outer reference scale is 180° which corresponds to nearly 20 000 km in (c) and (e), but only 14 000 km in (d) and (f) so that for the anomalies ((c) and (d)) $L_w \approx 30\,000$ km, 55 000 km, respectively. Also for the anomalies, the C_1 parameter is 0.12, 0.09 (0–30°N and 30°–60°N), respectively, i.e., slightly higher near the equator (see Table II). The bottom row ((e) and (f)) show the corresponding spatial analyses of the long term average rates from 1871 to 2012. The parameters are $C_1 \approx 0.17$, 0.13 and outer scales 30 000, 44 000 km, respectively, see Table III.

used vector norms corresponding to the isotropic special cases, adequate for our present purposes). To extend this to weather regime space-time processes, we need only to take into account causality and, if needed, anisotropy.

To extend this from the weather to the macroweather regime (including the transition between them) it suffices to assume that a multiplicative cascade starts at a scale L_w in space, but at a scale τ_c much larger than τ_w in time: the EFIF model (see the schematic of Fig. 5(a)). To see this, write the weather-macroweather flux $\varphi_{w,mw}$ (subscripts "w" and "mw"), here for precipitation (see Eqs. (3) and (9)) in terms of its "generator" $\Gamma_{w,mw}(\underline{r}, t)$

$$\varphi_{w,mw}(\underline{r}, t) = e^{\Gamma_{w,mw}(\underline{r},t)}. \tag{11}$$

Γ is a scaling additive process so that φ is multiplicative (see Schertzer and Lovejoy (1987)). If Γ has the appropriate

TABLE III. A comparison of various spatial macroweather exponent estimates using the 20CR data in latitudinal bands between 0°–30°N and 30°–60°N over the period 1871–2012. $R(\underline{r},t)$ is the anomaly rain rate at position $\underline{r}$, time t; R_c is the climatological rainrate obtained by averaging over the entire length of the series and R_{raw} is the raw data (only annually detrended).

	0°–30°N			30°–60°N		
	$R(\underline{r},t)$ (anomaly)	$R_c(\underline{r})$ (mean)	$R_{raw}(\underline{r},t)$ (raw)	$R(\underline{r},t)$ (anomaly)	$R_c(\underline{r})$ (mean)	$R_{raw}(\underline{r},t)$ (raw)
C_1	0.12	0.17	0.18	0.09	0.13	0.13
α	1.7	1.4	1.5	2.0	2.0	2.0
Outerscale (km)	30 000	30 000	45 000	55 000	44 000	56 000

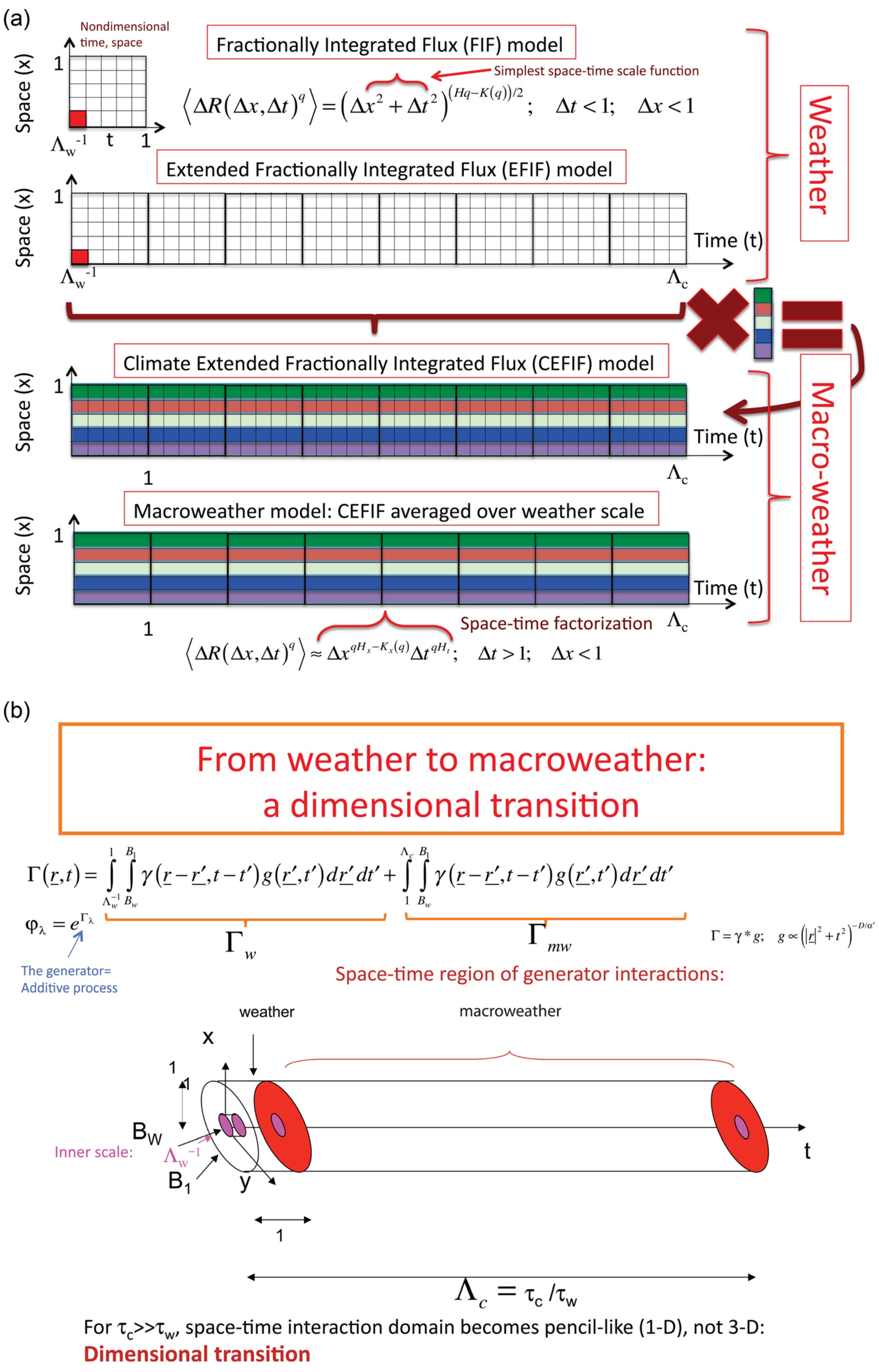

FIG. 5. (a) A schematic diagram showing time and a single spatial dimension for the FIF model (top), EFIF (second from top), CEFIF (third), and CEFIF averaged over macroweather (bottom). Space and time are nondimensionalized using the planetary scale L_w for space, and the corresponding weather time scale $\tau_w = \varepsilon^{-1/3}L_w^{2/3}$ so the weather/macroweather transition occurs at $t=1$ and $x \le 1$. Also indicated are the basic forms of the space-time (generalized, qth order structure function) statistics with the CEFIF model having space-time factorization. (b) A schematic diagram showing the weather and macroweather regions of integration for the cascade convolution (Eq. (12)) in horizontal-time space (x,y,t) nondimensionalized by using the size of the earth and the lifetime of planetary structures. B_1 is the space-time region corresponding to weather processes ($r<1$, $t<1$; $r=(x^2+y^2)^{1/2}$) and B_w is the corresponding inner (dissipation) scale, size Λ_w^{-1} (a factor Λ_w times smaller). The cylindrical region between the red (dark, larger, filled) circles is macroweather region with $r<1$, $\Lambda_c>t>1$; in this region, the temporal variability dominates the integral since the convolution kernel g is nearly independent of r (γ is an i.i.d. Levy noise subgenerator representing the innovations). Adapted with permission from Lovejoy, S. and D. Schertzer, *The Weather and Climate: Emergent Laws and Multifractal Cascades* (Cambridge University Press, 2013). Copyright 2013 Cambridge University Press.

scaling, then φ will satisfy Eq. (9) of a multiplicative cascade, it will follow the behavior in Figs. 4(a) and 4(b). For this, we require

$$\Gamma = N\gamma * g; \quad g(\underline{r},t) = \Theta(t)[\![(\underline{r},t)]\!]^{-d/\alpha}; \\ [\![(\underline{r},t)]\!] = |(\underline{r},t)| = (|\underline{r}|^2 + t^2)^{1/2}, \tag{12}$$

where "*" indicates space-time convolution over the entire region for which the cascade occurs. In Eq. (12), N is a normalization factor and γ is a Levy noise subgenerator index α made up of independent identically distributed random variables representing the "innovations," $d=3$ is the dimension of (horizontal) space-time and Θ(t) is the Heaviside function ($=0$ for $t<0$, $=1$ for $t \geq 0$) needed to take causality into account (see Marsan *et al.* (1996) and chap. 9 in Lovejoy and Schertzer (2013)). $[\![\underline{r}, t]\!]$ is a space-time scale function; although it can be quite general we have chosen the simplest possible consistent with the isotropic symmetry in Eq. (7) (i.e., the norm of the vector ($\underline{r}$,t)). Space and time were nondimensionalized using the planetary scale L_w distances and the lifetime of planetary structures τ_w. Fuller details are given in Subsection 1 of the Appendix.

Figure 5(b) shows a schematic of the region of integration: it can be seen that for the convolution in Eq. (12), the domain of integration can be separated into two statistically independent terms as

$$\Gamma_{w,mw}(\underline{r},t) = \Gamma_w(\underline{r},t) + \Gamma_{mw}(\underline{r},t), \tag{13}$$

where the weather and macroweather generators are

$$\Gamma_w(\underline{r},t) = \int\limits_{\Lambda_w^{-1} \leq |\underline{r}| \leq 1} \int\limits_{\Lambda_w^{-1}}^{1} g(\underline{r}-\underline{r}', t-t')\gamma(\underline{r}',t')dt'd\underline{r}', \\ \Gamma_{mw}(\underline{r},t) = \int\limits_{\Lambda_w^{-1} \leq |\underline{r}| \leq 1} \int\limits_{1}^{\Lambda_c} g(\underline{r}-\underline{r}', t-t')\gamma(\underline{r}',t')dt'd\underline{r}'. \tag{14}$$

In the above, the weather generator Γ_w is obtained by integrating over the space-time region corresponding to weather processes ($\Lambda^{-1}{}_w \leq r \leq 1$, $t \leq 1$; $r = |\underline{r}| = (x^2+y^2)^{1/2}$) down to dissipation scales (indicated B_1 and B_w in Fig. 5(b) which is the corresponding inner (dissipation) scale, size $\Lambda_w{}^{-1}$ (a factor Λ_w times smaller). The macroweather generator Γ_{mw} is obtained from the cylindrical region between the red circles, i.e., the region with $\Lambda_w{}^{-1} \leq r \leq 1$, $\Lambda_c \geq t \geq 1$; in this region (denoted "M" in the Appendix), the temporal variability dominates the integral since the convolution kernel g is nearly independent of r. $\Lambda_\mathrm{w}{}^{-1}$ is the inner scale ratio of the weather processes and $\Lambda_\mathrm{c} = \tau_\mathrm{c}/\tau_\mathrm{w}$ is the outer scale ratio of the temporal cascade. The first term on the right of Eq. (13) (Γ_w) corresponds to a roughly isotropic space-time region so that all the degrees of freedom (the γ's) are important in the left most integral and—due to the astute choice of exponent in Eq. (12) (d/α)—the weather regime statistics follow the multiplicative cascade law in Eq. (9) with $K(q)$ given by Eq. (10) (the value of C_1 is determined by N, see Subsection 1 of the Appendix for a review). However, the macroweather term (the second term on the right in Eq. (13)) is pencil-like, and over the macroweather range of temporal integration $t \geq 1 \geq r$ so that $g(\underline{r},t) \approx \Theta(t)t^{-d/\alpha}$ and hence it is mostly the temporal degrees of freedom that are effective, the spatial degrees of freedom are essentially "quenched"; the system is essentially reduced in dimension from a $2+1$ horizontal space, time to a 1 dimensional system (time), a "dimensional transition" (Lovejoy and Schertzer, 2010c).

Exponentiating the generators, we obtain the following multiplicative relationship for the fluxes:

$$\varphi_{w,mw}(\underline{r},t) = \varphi_w(\underline{r},t)\varphi_{mw}(\underline{r},t); \quad \varphi_{w,mw}(\underline{r},t) = e^{\Gamma_{w,mw}}; \\ \varphi_w(\underline{r},t) = e^{\Gamma_w}; \quad \varphi_{mw}(\underline{r},t) = e^{\Gamma_{mw}}. \tag{15}$$

Due to the quenching, we see that the macroweather flux has practically no variability at nondimensional space or time scales <1 (i.e., smaller than L_w, shorter than τ_w), thus

$$\varphi_{w,mw}(\underline{r},t) = \varphi_w(\underline{r},t)\varphi_{mw}(t). \tag{16}$$

If we now average this equation over nondimensional time-s $=1$ (i.e., over time scales up to τ_w), due to the space-time coupling in the weather regime, this temporal averaging effectively averages out much of the spatial variability as well so that

$$\varphi_{w,mw,\tau}(\underline{r},t) = \varphi_{mw}(t); \quad \tau_w < \tau < \tau_c\,, \tag{17}$$

where $\varphi_{w,mw,\tau}(\underline{r},t)$ is the temporally averaged flux over a scale $\tau > \tau_w$. Strictly speaking, φ_{mw} is simply more slowly varying in space than in time so that $\varphi_{mw}\ (\underline{r},\ t) \approx \varphi_{mw,\tau}\ (t)$ and Eqs. (16) and (17) should be interpreted as indicating that the type of temporal statistical process is the same at all spatial locations, this will be clarified in Subsection III D and in the Appendix. Figure 6(a) shows a realization of the EFIF model averaged over the model weather scales: 64 neighbouring points 1024 pixels in time (each of duration τ_w), compare this with the data in Fig. 2(b) and see Section III D for more details.

From this analysis and Fig. 6(a), we see that a single weather/macroweather cascade model will yield macroweather fields that are smoother in space than in time, even though empirically, the data show the converse: strong multifractal spatial variability but nearly quasi-Gaussian temporal variability (see, e.g., Table II, and Figs. 4(a)–4(f)). This led Lovejoy and Schertzer (2013) to propose that models of atmospheric variability valid in the macroweather regime must include an additional temporally slowly varying space-time climate process $\varphi_c(\underline{r},t)$ (that only varies significantly at long time scales $\tau > \tau_c$), the consequence of physically different climate processes. The full (weather-macroweather-climate) model is thus

$$\varphi_{w,c}(\underline{r},t) = \varphi_{w,mw}(\underline{r},t)\varphi_c(\underline{r},t). \tag{18}$$

Since by definition for time scales $<\tau_c$, the climate process has $\varphi_c(\underline{r},t) \approx \varphi_c(\underline{r})$, over the macroweather regime, we find

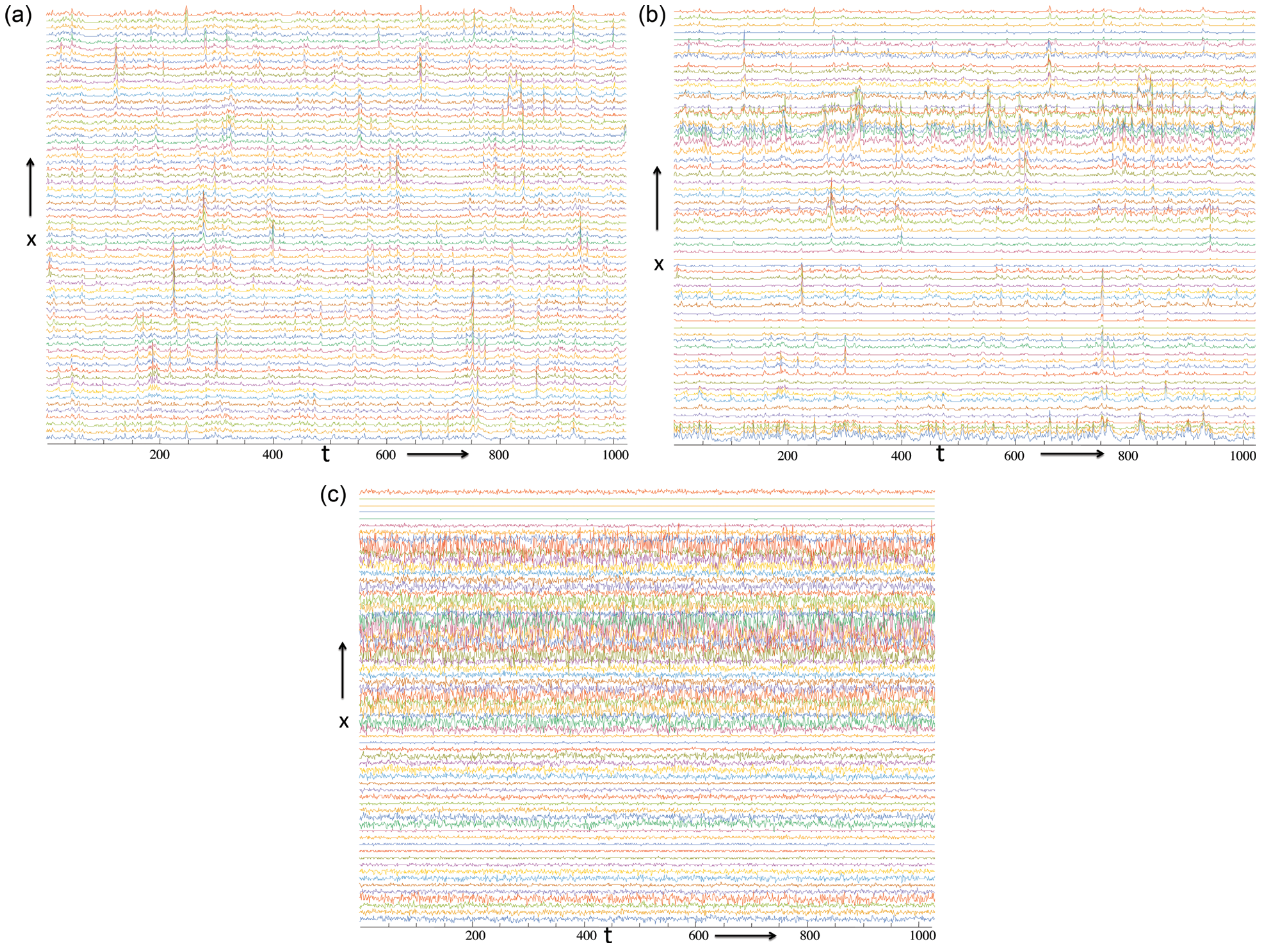

FIG. 6. (a) EFIF model with parameters given in Table IV, time series as a function of spatial location (x). The plot shows 64 neighbouring pixels in space (bottom to top) and 1024 consecutive macroweather time units obtained by averaging at the model scale τ_w. Notice that there is little spatial variability: from bottom to top, the series are statistically very similar to each other. Compared to the data (Fig. 2(b)) the spatial variability is too low. (b) The CEFIF model with parameters given in Table IV, obtained by multiplying the temporally averaged EFIF model shown in Fig. 6(a) by a purely spatial climate process. One can see that the resulting spatial variability (the variation from series to series) is much more realistic (see the data graph, Fig. 2(b) and see Table IV for the scaling exponents). (c) The SLIMM model with parameters $H_t = -0.4$, $H_x = -0.2$ (Table I), $C_{1x} = 0.1$, Table II, also $\alpha_x = 1.8$. We see that while each series has the same type of temporal variability (fractional Gaussian noise, fGn), that the amplitude of the series to series variability clusters due to the multifractal spatial climate process. Compare this with the data (Fig. 2(b)) and with the EFIF and CEFIF realizations ((a) and (b)).

$$\varphi_{w,c,\tau}(\underline{r},t) = \varphi_{mw}(t)\varphi_c(\underline{r}); \quad \tau_w < \tau < \tau_c, \tag{19}$$

where $\varphi_{w,c,\tau}(\underline{r},t)$ is the full space-time weather-climate process averaged over time scale τ and the equality is in the sense of random variables. See Fig. 6(b) for a realization and Section III D for more details. This is the macroweather space-time factorization property of the fluxes, it is compatible with the scaling and it is predicted by this simple model. Since the observables (e.g., the precipitation rate) are obtained by fractional integration (power law filters, order H) of the fluxes, we obtain equivalent space-time factorizations of the observables. Physically, the interpretation is that the macroweather spatial variations are associated with different climate zones but that each zone has the same statistical type of temporal variability whose origins are in high frequency weather dynamics. In other words, the climate spatially modulates the atmosphere at macroweather scales even though the climate temporal variations are at longer scales. This argument is admittedly hand-waving and is justified more mathematically in Subsection 2 of the Appendix where it is found that factorization is only an approximate symmetry of the EFIF model, although in Sec. III F we show that it is empirically valid to a very good approximation; indeed, it provides the theoretical basis of many otherwise *ad hoc* "homogenization" techniques.

D. Numerical investigation of the EFIF based weather-climate process: CEFIF

In Appendix 10A of Lovejoy and Schertzer (2013), the temporal macroweather structure of the EFIF model was investigated and it was found to be "pseudo-scaling"; the autocorrelations drop off with a (leading) Δt^{-1} behavior. Such behavior is singular so that, for example, spectra have characteristics that depend on both the high and low frequency cutoffs—i.e., the range of macroweather scales. The result was that the process had roughly the low intermittency $H < 0$ behavior characteristic of the macroweather regime with the value of H depending on the range of scales, and being nearly independent of the weather regime C_1, α, and H parameters. While this analysis clarified some of the statistical properties of the EFIF model, it did not address the spatial variability issue nor did it provide a more convincing (mathematical) investigation of the factorization property. The mathematical difficulties in analyzing the EFIF model are underscored in the Appendix that sheds light on the origins of factorization and the fact that although it is not an exact symmetry, it is only weakly broken.

We therefore turn to a numerical investigation of both EFIF properties as well as the weather-climate model described in Sec. III C, which is obtained by multiplying the EFIF process by a purely spatially varying (climate scale) multifractal process. As usual, we are interested in the scaling properties (exponents) and therefore require the largest possible range of scales, in this case we considered a single realization of a $2^7 \times 2^7 \times 2^{12}$ (x,y,t) EFIF process with a corresponding $2^7 \times 2^7$ (x,y) climate process (x and y are spatial coordinates). The results are shown in Table IV, below we discuss the table row by row, and Figs. 6(a) and 6(b) show sample realizations of the process. All the parameters in the table are estimated using Haar fluctuation analysis on the simulation.

Each pixel represents about 40 000/128 ≈ 300 km, and in time 10 days/128 ≈ 2 h, the overall simulation therefore lasts about 1 year (about $4096/128 = 32\tau_w$). The simulation is the product of two independent processes: EFIF weather-macroweather process $\varphi_{w,mw}(x,y,t)$ and a pure cascade climate process $\varphi_c(x,y)$; the result is a Climate Extended Fractionally Integrated Flux process (CEFIF): $\varphi_{w,c}(x,y,t) = \varphi_{w,mw}(x,y,t)\ \varphi_c(x,y)$. For $\varphi_{w,mw}(x,y,t)$ and $\varphi_c(x,y)$, we took realizations with nominal parameters $\alpha = 1.8$, and $C_1 = 0.3$, 0.1, respectively (compare this to the numerically estimated C_1 parameters in rows 1 and 9). These parameters are "nominal" in the sense that they are the exponents from an infinite ensemble of statistically identical processes over wide ranges of scales (notice also that the H values in rows 1 and 9 of Table IV are not exactly 0 which is their ensemble average value). In comparison, we considered only a single realization with a modest range of scaling. In addition, there are "finite size" numerical issues from the simulation at both the largest and smallest scales (see Lovejoy and Schertzer (2010a; 2010b)). The limitations of the model can, for example, be seen from the fact that the $K(q)$ function of the product of two independent processes is the sum of the individual $K(q)$ functions, so that the corresponding C_1's also add. Therefore, we expect $C_{1wc,space} = 0.3 + 0.1 = 0.4$, and since $\varphi_c(x,y)$ has no time dependence, $C_{1wc,time} = 0.3$. Notice (row 5) that this is more or less verified to within the available numerical precision (a single simulation over a finite range of scales). Note that since $\varphi_c(x,y)$ has no time dependence, the temporal exponents (rows 1–4) of the EFIF and CEFIF models are identical.

Recall that in cascades, the fluxes are conserved from one scale to another so that $H = 0$. Both $\varphi_c(x,y)$ as well as $\varphi_{w,mw}(x,y,t)$ in its weather regime (i.e., to time scales less than 128 pixels) therefore have $H = 0$; in the macroweather regime, due to the quenching of the spatial degrees of freedom, the flux is no longer conserved across scales so that $H < 0$ (see rows 3, 4, and 8 and the Appendix). Therefore, in these regimes (rows 1, 4, 5, 7, and 9), the $H \neq 0$ results are model artefacts. In the macroweather regime however, there are nontrivial H values. First, in rows 2 and 3: $H_t \approx -0.3$ and -0.4 for pixel and global scales; although these are close to the observations ≈−0.4, as mentioned above, they are somewhat sensitive to the macroweather range of scales which here is only over the scale range $2^{12}/2^7 = 2^5$. Second, in row 6, the spatial macroweather exponent $H_x \approx -0.2$ is a bit higher than H_t so that the spatial macroweather is indeed a bit smoother than temporal macroweather. However, if the CEFIF weather-climate model is correct, the EFIF value $H_x \approx -0.2$ is not directly measurable since the spatial variability is dominated by the $H_x = 0$, $\varphi_c(x,y)$ process (right hand columns, row 9) with realistic C_1 value (row 9 far right data column). Third, in row 8 for the macroweather anomalies, we have $H_x \approx -0.2$ which is again close to the GHCN value (Fig. 8(a)) but only agrees with the large scale 20CR, Smith values (Table I and Figs. 8(b) and 8(c)).

Overall, it is notable that most of the statistics are surprisingly close to those of real precipitation even though the numerics are for the precipitation flux (which is not necessarily the same as the precipitation *rate*) and we could easily justify the use of extra fractional integrations to yield R from φ. Such integrations could, for example, increase the weather regime H_t value from 0 in this flux model to ≈0.15 (CPC data, row 1) and could also increase the macroweather and climate values (rows 6 and 7) that are also too low (but which are poorly estimated from the 20CR and Smith data). Indeed, we have reasonably reproduced H, C_1 values in rows 1, 2, 3, 5, 6, 7, 8, and 9. Even if we discount these exceptions, 4 model exponents (H_w, C_{1w}, H_c, and C_{1c}) have predicted 4 additional precipitation exponents ($H_{mw,t}$, $C_{1mw,t}$, $C_{1mw,x}$, and $C_{1c,x}$) over wide ranges of space-time scales so that the CEFIF model is quite successful.

E. Directly Modelling macroweather: Multifractal SLIMM

1. Fractional Gaussian noise and the SLIMM model

The macroweather regime numerics of the EFIF and CEFIF model combined with the theoretical developments outlined in the Appendix show that while they seem to be fairly realistic, the macroweather statistics are theoretically difficult to handle. In particular, although the empirical temporal macroweather statistics are apparently fairly simple—nearly quasi Gaussian (small C_1) and with $H_t < 0$, the EFIF model is not simple. In addition, in order to model the macroweather regime, both models require a significant range of scales in the weather regime and this is numerically costly. This is analogous to the usual numerical climate modeling problem, whereby essentially weather models are integrated at time steps of several minutes and at fine (≈100 km) spatial resolutions only to be subsequently averaged to yield climate statistics. Therefore, in order to allow for practical applications such as macroweather precipitation forecasting, let us make a pure macroweather model with the minimum ingredients necessary to at least approximately reproduce both the CEFIF model and the empirical analyses. The resulting ScaLIng Macroweather Model (SLIMM) can be used to exploit the long range memory of the system and make stochastic forecasts (see Lovejoy *et al.* (in press)).

TABLE IV. The results of the Extended Fractionally Integrated Flux (EFIF) and Climate EFIF (CEFIF) models for the weather-climate process compared with precipitation data. The weather-macroweather model was on a $128 \times 1\,28 \times 4096$ grid (x,y,t), spatially periodic on a torus, causal in time. Thus each pixel represents about $40\,000/128 \approx 300$ km, and in time about 2 h, the overall simulation lasting about 1 year (about $4096/128 = 32\tau_w$). For the temporal statistics (the upper block with four rows of exponents), there is no theoretical difference between the Weather and Weather-Climate since the climate process has no time evolution, the small discrepancies are due to limited statistics. When the description indicates "pixel" it just means at the full space-time resolution, there was no averaging in space or in time. Time averaging is indicated with a subscript "τ" indicating the duration, the spatial averaging is indicated by overbars. Since these are fluxes, the nominal simulation values of the two $\varphi_{w,mw}(x,y)$ and $\varphi_c(x,y)$ had $H=0$ and $\alpha = 1.8$, the C_1 values were 0.3 and 0.1, respectively. See Fig. 2(c) for a sample of the data and Figs. 6(a) and 6(b) for realizations of the EFIF and CEFIF models.

				Weather ($\varphi_{w,mn}$) (EFIF)			Weather-climate ($\varphi_{w,c}$) (CEFIF)			Data	
	Row	Regime	Resolution	Symbol	H	C_1	Symbol	H	C_1	H	C_1
Time	1	Weather (pixel)	Single pixel[a]	$\varphi_{w,mw}$	–0.06	0.31	$\varphi_{w,c} = \varphi_{w,mw}\varphi_c$	–0.06	0.31	0.15[b]	0.30 ± 0.07[c]
	2	Macroweather (pixel)	Averaged 128 pixels in time[d]	$\varphi_{mw} = \varphi_{w,mw,\tau_w}$	–0.30	0.09	$\varphi_{mw}\varphi_c$	–0.30	0.09	–0.4[e]	0.01–0.02[f]
	3	Macroweather (global)	Averaged 128 × 128 × 128 pixels in space, time[g]	$\overline{(\varphi_{mw})}_{space}$	–0.42	0.04	$\overline{(\varphi_{mw}\varphi_c)}_{space}$	–0.42	0.04	–0.4[h]	0.01–0.02[h]
	4	Weather (global)	Averaged 128 × 128 pixels in space[i]	$\overline{(\varphi_{w,mw})}_{space}$	0.07	0.11	$\overline{(\varphi_{w,mw}\varphi_c)}_{space}$	0.07	0.11	…	…
Space	5	Weather	Single pixel[j]	$\varphi_{w,mw}$	0.00	0.34	$\varphi_{w,c} = \varphi_{w,mw}\varphi_c$	0.03	0.42	0.0[k]	0.39 ± 0.10[c]
	6	Macroweather	Averaged 128 pixels in time[l]	$\varphi_{mw} = \varphi_{w,mw,\tau_w}$	–0.22	0.04	$\varphi_{mw}\varphi_c$	0.03	0.13	0.1–0.2[m]	0.14 ± 0.05[c]
	7	Climate	Averaged 4096 pixels in time[n]	φ_{mw,τ_c}	0.02	0.02	$\varphi_c \approx \varphi_{w,c,\tau_c}$	0.06	0.11	0.1–0.2[o]	0.15±0.02[p]
	8	Macroweather	Anomaly (difference)	…	…	…	$\varphi_c(1-\varphi_{mw})$	–0.16	0.10	–0.2[q]	0.10
Climate process[r]	9		Single pixel	…	…	…	φ_c	0.03	0.12	0.15–0.2[o]	0.15 ± 0.02[p]

[a] Fit over weather range, i.e., to $\approx \tau_w = 128$ time units; the nominal theoretical parameters were $H=0$, $C_1 = 0.3$, the differences in this row are due to inadequate statistics (the use of only a single realization as well as finite size effects—at both small and large scales—in the numerics).

[b] This value is from the weather regime in Fig. 1. However, its value is not robust since it is sensitive to zero and low rain rates.

[c] The average and standard deviation of all the relevant estimates from Table II. Note that the time and space values of C_1 are different by about 0.1 as is theoretically expected since the space has the extra variability due to multiplication by φ_c.

[d] See Eq. (17); as shown in Lovejoy and Schertzer (2013), Appendix 10A, the key macroweather temporal exponent H_t depends on the range of scales τ_c, Λ_c. For comparison, the analogous (numerically estimated) H_t macroweather exponent for Λ_c 8 times longer (i.e., 512 pixels, not 64), yields -0.17 ± 0.10 where the variation is pixel to pixel; the corresponding value for the simulation here is -0.38 ± 0.25 (the standard deviation is the pixel to pixel spread, the difference with the value in the table is because the latter is a fit to the ensemble statistics). These numbers should be compared to the empirical pixel by pixel H_t estimates -0.41 ± 0.07, -0.38 ± 0.09, and -0.43 ± 0.10 for GHCN, 20CR, and Smith, Sec. II C.

[e] See Table I.

[f] GHCN, 20CR, and Smith, from Table I.

[g] Averaged over all space, fit over the macroweather range of 300–2048 time units, this is same as space and time averaged to macroweather scales.

[h] GHCN, 20CR, and Smith, from dLL.

[i] Averaged over all space, but fit to weather regime (16–250 time units). Globally averaged precipitation products at high enough frequency do not exist.

[j] Fit over weather range; theory: $H=0$, $C_1 = 0.4$.

[k] This value is from TRMM radar study (Lovejoy *et al.*, 2008), but is sensitive to zero and low rain rate issues.

[l] Averaged over the weather scales (a bit further, to 512 time units).

[m] The raw 20CR, Smith, values from Table I (see Figs. 8(b) and 8(c)). This cannot be estimated from GHCN which has only anomalies.

[n] The weather climate process is not sensitive to the averaging length, but the weather only process has H that depends somewhat on the temporal averaging length.

[o] This is the raw long term value (the bottom of the top set of curves in Figs. 8(b) and 8(c)).

[p] 20CR, Table III, average of the 0°–30° N and 30°–60° N values.

[q] From GHCN, Fig. 8(a). The anomalies from the 20CR and Smith data have both $H_x \approx +0.1$, 0.2 regions (less than ≈ 4000–7500 km) and regions close to -0.2 (slope $\xi(2)/2 \approx -0.3$ indicated at large spatial scales in Figs. 8(b) and 8(c). The large scale value ($H_x = -0.2$) in common with the GHCN anomaly value was thus taken as the most likely true value.

[r] This is a space only process, the nominal theoretical parameters were $H=0$, $C_1 = 0.15$.

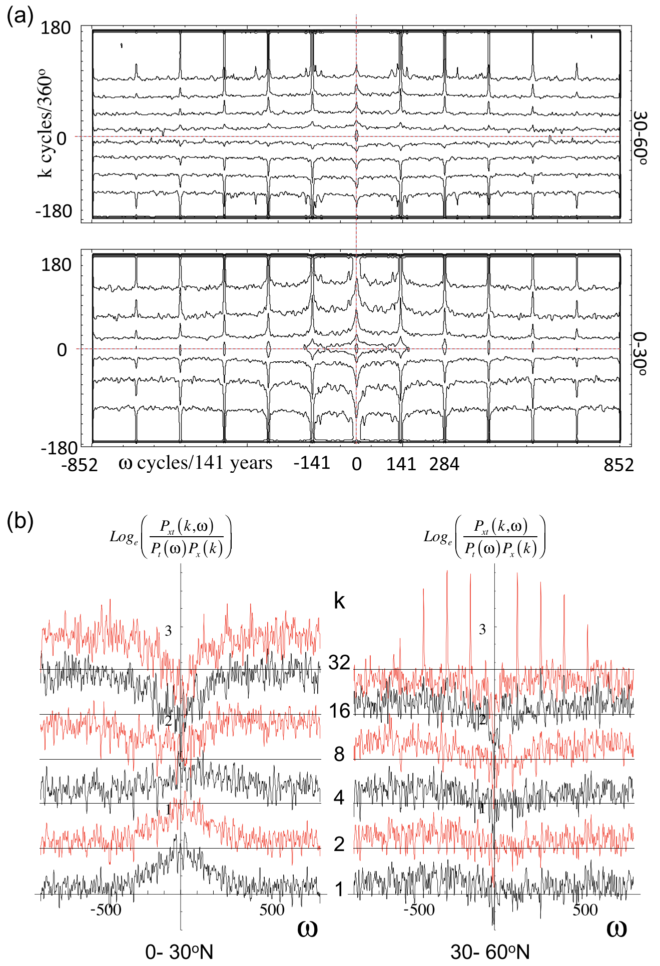

FIG. 7. (a) The space-time spectral densities $P_{xt}(k,\omega)$ for the 20CR monthly precipitation product over the period of 1871–2012. The horizontal axis is for the frequencies (in units of cycles/141 years), the vertical axes are for the zonal wavenumbers (up to ±180° longitude). Contours of the spectral densities for latitudes 0° to 30°N, and 30° to 60°N are shown on bottom and top. Note the annual cycle and the harmonics (the regularly spaced spikes). Note that the contour lines are generally parallel to the axes as expected by the factorization property. (b) A direct test of the factorization hypothesis for the spectra analysed in (a). Each line shows the ratio of zonal wavenumber–frequency spectral density $P_{xt}(k,\omega)$ to the product of the zonal only $P_x(k)$ and frequency only $P_t(\omega)$ densities for zonal wavenumbers increasing in octaves from bottom to top. Each section is displaced by a factor $e^{0.5}$ in the vertical and the shading alternates for clarity. The frequency units are $(\text{months})^{-1}$ and the wavenumber units are cycles per half-circumference (due to the latitudinal dependent map factor, about 20 000 km on the left, about 14 100 km on the right). The constancy of the ratio is remarkable when it is considered that the total variation (maximum/minimum) of $P_{xt}(k,\omega)$ over the range of (k,ω) in this figure is $\approx 10^7$.

In the temporal domain, we take the simplest nonintermittent model—a Gaussian—so that we pay special attention to the second order statistics characterized by autocorrelation functions ("c"). With this Gaussian approximation, and since $-1<H<0$, we are led to the fractional Gaussian noise (fGn) process

$$G_H(t)=\frac{k_H}{\Gamma(1/2+H)}\int_{-\infty}^{t}(t-t')^{-(1/2-H)}\gamma(t')dt';\ \ H<0, \quad (20)$$

where Γ is the usual gamma function (not to be confused with the cascade generator) and k_H is a constant (see below). The innovations γ are taken as zero mean ($\langle\gamma(t)\rangle=0$) Gaussian white noise processes having an autocorrelation

$$c_\gamma(\Delta t)=\langle\gamma(t-\Delta t)\gamma(t)\rangle=\delta(\Delta t), \quad (21)$$

so that γ is a temporally "delta correlated" Gaussian white noise process, the integration in Eq. (20) is a temporal fractional integral of order $\frac{1}{2}+H$ of γ (by inspection, we see that it is causal since the process at time t depends only on the innovations for $t'<t$). While at each point in space, G_H is an fGn process; its (order one) time integral is a (more familiar) fractional Brownian motion with parameter $1+H$.

If we define the τ resolution process by averaging $G_{H,\tau}(t)=\frac{1}{\tau}\int_{t-\tau}^{t}G_H(t')dt'$ and we define the constant $k_H=\left(\frac{\pi}{2\cos(\pi H)\Gamma(-2H-2)}\right)^{1/2}$, we obtain the simple and exact result for the resolution τ autocorrelation function

$$\begin{aligned}c_{G,\tau}(\Delta t)&=\langle G_{H,\tau}(t)G_{H,\tau}(t-\Delta t)\rangle\\&=\frac{\tau^{2H}}{2}\left[(\lambda+1)^{2H+2}+(\lambda-1)^{2H+2}-2\lambda^{2H+2}\right];\\\lambda&=\frac{\Delta t}{\tau};\quad \lambda\ge 1;\quad -1<H<0\end{aligned} \quad (22)$$

which for large Δt is

$$c_{G,\tau}(\Delta t)\approx(H+1)(2H+1)\Delta t^{2H};\quad \Delta t\gg\tau;\quad -1<H<0 \quad (23)$$

and the variance ($c_{G,\tau}(0)$)

$$\langle G_{H,\tau}(t)^2\rangle=\tau^{2H};\quad -1<H<0, \quad (24)$$

these results are reviewed in Lovejoy *et al.* (in press) (for a full mathematical overview see Biagini *et al.* (2008)). From Eq. (24), we see that fGn diverges in the small scale limit ($\tau\to 0$). Also, since G_H is a Gaussian with mean zero and $H<0$, the fluctuation over scale τ is equal to the mean anomaly, itself equal to $G_{H,\tau}$ so that in the previous "Δ" notation for fluctuations, $\Delta G_H(\tau)=G_{H,\tau}$. Finally, the variance and autocorrelation function determine all the one and two point statistics (including the qth order moments), so that we obtain for the structure function

$$\langle|G_{H,\tau}|^q\rangle=\langle|\Delta G_H(\tau)|^q\rangle\propto\tau^{\xi(q)};\quad \xi(q)=qH;\quad -1<H<0 \quad (25)$$

(independent of t since G_H is statistically stationary). We use Eq. (25) below.

The extension to spatial processes is straightforward, although many options are possible. The simplest is to assume statistical isotropy in d spatial dimensions and to integrate over all space

$$G_H(\underline{r})=\frac{k_{H,d}}{\Gamma(d/2+H)}\int_{\mathbb{R}^d}|\underline{r}-\underline{r}'|^{-(d/2-H)}\gamma(\underline{r}')d^d\underline{r}';\quad -1<H<0, \quad (26)$$

where the constant $k_{H,d}$ depends on d (k_H, given above, was the causal $d=1$ value) and where γ is delta correlated in space

$$c_\gamma(\underline{\Delta r}) = \langle \gamma(\underline{r} - \underline{\Delta r})\gamma(\underline{r})\rangle = \delta(\underline{\Delta r}). \quad (27)$$

We can now combine the spatial and temporal fractional integrations to obtain the space-time fractional Gaussian noise model

$$\varphi_{mw}(\underline{r}, t) = \frac{k_{H_x,d}}{\Gamma(d/2 + H_x)} \frac{k_{H_t,1}}{\Gamma(1/2 + H_t)} \int\limits_{\mathbb{R}^d} \int\limits_{-\infty}^{t} |\underline{r} - \underline{r}'|^{-(d/2-H_x)} \times (t - t')^{-(1/2-H_t)} \gamma(\underline{r}', t') dt' d^d \underline{r}'; \quad -1 < H_t < 0; \quad -1 < H_x < 0 \quad (28)$$

φ_{mw} is a model of the pure macroweather process, i.e., valid only at time scales $> \tau_w$ and not taking into account any spatial or temporal variability due to climate scale processes. In Eq. (28), $\gamma(\underline{r},t)$ is a delta correlated space-time noise

$$c_\gamma(\underline{\Delta r}, \Delta t) = \langle \gamma(\underline{r} - \underline{\Delta r}, t - \Delta t)\gamma(\underline{r}, t)\rangle = \delta(\underline{\Delta r})\delta(\Delta t). \quad (29)$$

For the process averaged at spatial resolution l and temporal resolution τ, the autocorrelation is therefore

$$c_{\varphi,mw}(\underline{\Delta r}, \Delta t) \propto |\underline{\Delta r}|^{2H_x} \Delta t^{2H_t}; \quad |\underline{\Delta r}| \gg l; \quad \Delta t \gg \tau; \quad -1 < H_x < 0; \quad -1 < H_t < 0, \quad (30)$$

i.e., ignoring constant factors (see Eq. (23)).

At the same time, the amplitude of the fluctuations at resolution l, τ is

$$\langle |\varphi_{mw,l,\tau}|^q \rangle \propto l^{\xi_x(q)} \tau^{\xi_t(q)}; \quad \xi_x(q) = H_x q; \quad \xi_t(q) = H_t q; \quad -1 < H_x < 0; \quad -1 < H_t < 0 \quad (31)$$

(see Eq. (24); the constants in Eq. (28) are chosen so that the proportionality becomes an equality in the case $q = 2$ and note the special case: $\langle \varphi^2_{mw,l,\tau} \rangle = c_{\varphi,mw}(0,0)$). From Eqs. (30) and (31), we see that the statistics $\langle |\varphi_{mw,l,\tau}|^q \rangle$ satisfy the space-time factorization property.

From row 6, Table IV, we see that the EFIF spatial macroweather behaviour is itself not far from a fractional Gaussian noise (c.f. row 6 with $H_x \approx -0.2$, $C_{1x} \approx 0$, i.e., somewhat smoother than the corresponding values $H_t \approx -0.3$, -0.4, $C_{1t} \approx 0$—rows 2 and 3—but still not really smooth). If this is correct, it would imply that we could take $c_{\varphi,mw}(\underline{\Delta r}, \Delta t) = |\underline{\Delta r}|^{2H_x} \Delta t^{2H_t}$ with $H_t = -0.4$, $H_x = -0.2$, see also the empirical values in Table II which are close.

From Eq. (23) and since $\langle \gamma(\underline{r}, t) \rangle = 0$ and $H_t < 0$, we see that long time averages of φ_{mw} will converge to zero (recall that since $H_t < 0$, the averages are good definitions of fluctuations). Therefore, this is a model for precipitation *anomalies*; we return to this below.

Since the structure function exponents are linear (Eq. (31)) we have $K_x(q) = K_t(q) = 0$, so that the process is not cascade-like. In time, this behaviour is a reasonable approximation since $C_{1t} \approx 0$; however in space, we saw that the empirical behavior is reasonably intermittent, multifractal behavior with $C_{1x} \approx 0.15$ (see Tables II and IV), and the space-time statistics separate into spatial and temporal factors. Hence as in the CEFIF model, we multiply the process by the flux of a conservative "climate regime" cascade φ_c

$$\langle \varphi_{c,l}(\underline{r})^q \rangle \approx \lambda^{K_x(q)} \propto l^{-K_x(q)}; \quad \lambda = \frac{L_w}{l}, \quad (32)$$

where λ is the scale ratio of the outer cascade scale L_w to the resolution l (in this theoretical discussion, for simplicity, we take $L_{eff} = L_w$). The corresponding correlation function is

$$c_{c,l}(\underline{\Delta r}) = \left(\frac{|\underline{\Delta r}|}{l}\right)^{-K_x(2)}; \quad |\underline{\Delta r}| > l \quad (33)$$

(where for simplicity we have assumed that the process is statistically isotropic, the horizontal scale depends on the vector norm which is isotropic).

As above, the overall model for the flux is thus the product of the climate process with the macroweather process

$$\varphi_{w,c,l,\tau}(\underline{r}, t) = \varphi_{c,l}(\underline{r})\varphi_{mw,l,\tau}(\underline{r}, t) \quad (34)$$

(here and below we neglect the very slow temporal variability of the climate process so that we take $\varphi_{c,l}(\underline{r})$), so that

$$\langle |\varphi_{w,c,l,\tau}(\underline{r}, t)|^q \rangle = \langle |\varphi_{c,l}(\underline{r})|^q \rangle \langle |\varphi_{mw,l,\tau}(\underline{r}, t)|^q \rangle \propto l^{\xi_x(q)} \tau^{\xi_t(q)}; \quad \xi_x(q) = qH_x - K_x(q); \quad \xi_t(q) = qH_t; -1 < H_x < 0; \quad -1 < H_t < 0 \quad (35)$$

the autocorrelations also multiply

$$c_{w,c,l,\tau}(\underline{\Delta r}, \Delta t) = c_{c,l}(\underline{\Delta r}) c_{wm,l,\tau}(\underline{\Delta r}, \Delta t) = |\underline{\Delta r}|^{\xi_x(2)} \Delta t^{\xi_t(2)}. \quad (36)$$

Notice that by simple multiplication of the fractional Gaussian noise process with a conservative ($H = 0$) multifractal process ($\varphi_{c,l}$), we have obtained a process with an extra $K_x(q)$ term. This method only works because $H_x < 0$; if $H_x > 0$, then neither Eqs. (30), (31), (36) are valid and to obtain a process with linear part of $\xi_x(q) = qH_x - K_x(q)$ one must instead fractionally integrate $\varphi_{w,c,l,\tau}(\underline{r},t)$ (Eq. (34)) directly.

2. The precipitation anomaly process

Although $\varphi_{w,c}$ was obtained multiplicatively as a flux (essentially the fractional integration was done before the product was taken rather than afterwards as in the $H > 0$ turbulence FIF model), we can already take it as a model for the precipitation anomaly, hence we can take the dimensional process

$$R_{w,c,l,\tau}(\underline{r}, t) = \sigma_{anom} L_w^{-H_x} \tau_c^{-H_t} \varphi_{w,c,l,\tau}(\underline{r}, t) = \sigma_{anom} L_w^{-H_x} \tau_c^{-H_t} \varphi_{c,l}(\underline{r}) \varphi_{mw,l,\tau}(\underline{r}, t); \quad l \le L_w; \quad \tau_w \le \tau \le \tau_c, \quad (37)$$

where L_w and τ_c are the largest spatial and temporal scales over which the scaling is obeyed. If we take $l = L_w$, we have $\lambda = 1$ and $\langle |\varphi_{c,L_w}(\underline{r})|^q \rangle = 1$ (Eq. (32)) while $\langle \varphi_{mw,L_w,\tau_c}(\underline{r}, t)^2 \rangle = L_w^{2H_x} \tau_c^{2H_t}$ (Eq. (31)). We therefore see that σ_{anom} is the standard deviation of the largest scale anomalies: $\langle R_{w,c,L_w,\tau_c}(\underline{r}, t)^2 \rangle^{1/2} = \sigma_{anom}$ (also, since $\langle \varphi_{mw,L_w,\tau_c}(\underline{r}, t) \rangle = 0$, the mean anomaly is zero: $\langle R_{w,c,l,\tau}(\underline{r}, t) \rangle = 0$). From dLL, we find that for global series (i.e., scale L_w) and $\tau_c \approx 20$ years (the rough outer limit of the macroweather scaling regime) that $\sigma_{anom} \approx 1$ mm/month.

Figure 6(c) shows a realization of the resulting space-time SLIMM process in $d=1$ spatial dimensions. We can see that the realization is indeed quite similar to the CEFIF simulation (Fig. 6(b)) and the data (Fig. 2(b)) in that each location has the same type of variability but with amplitudes strongly varying from one location to another.

3. The raw precipitation process (anomaly plus climatological values)

$R_{w,c,l,\tau}(\underline{r},t)$ is a model of the anomalies, we also need to model the "raw" rain rate (i.e., the actual, absolute rainrate with only the annual cycle removed). Since the amplitude of $R_{w,c,l,\tau}(\underline{r},t)$ decreases with averaging, for large enough τ (but still small enough that we can ignore longer term, slow climate scale variations), we can take

$$R_{raw,l,\tau}(\underline{r},t) = R_{c,l}(\underline{r}) + R_{w,c,l,\tau}(\underline{r},t), \tag{38}$$

where $R_{c,l}(\underline{r})$ is the climatological average rain rate. From Figs. 4(c)–4(f), we saw that the long term average precipitation field (our estimate of the climatological rainrate $R_{c,l}(\underline{r})$) had very nearly the same spatial statistical variability (spatial exponents) as for the spatial anomalies, hence the simplest model for $R_{c,l}(\underline{r})$ is to take

$$R_{c,l}(\underline{r}) = \mu_{clim}\varphi_{c,l}(\underline{r}). \tag{39}$$

Since $\langle|\varphi_{c,L_w}(\underline{r})|^q\rangle = 1$ we see that μ_{clim} is the global scale, long term climatological rain rate: $\mu_{clim} = \langle R_{c,L_w}(\underline{r})\rangle$, according to the data in dLL, $\mu_{clim} \approx 80$ mm/month (differing only slightly between the Smith and 20CR global series).

By calculating the variance of the raw rainrate (Eq. (38)), we can now consider its overall statistical dependence on the space-time resolution

$$\langle R_{raw,l,\tau}(\underline{r},t)^2\rangle = \left(\frac{l}{L_w}\right)^{-K_x(2)}\left(\mu_{clim}^2 + \sigma_{anom}^2\left(\frac{l}{L_w}\right)^{2H_x}\left(\frac{\tau}{\tau_c}\right)^{2H_t}\right). \tag{40}$$

Equation (38) states that at any given space-time scale, the anomalies fluctuate about the climatological mean; if the typical fluctuations are larger than the mean, then the model implies impossible negative raw rainrates. According to Eq. (40), when $\mu_{clim} \gg \sigma_{anom}\left(\frac{l}{L_w}\right)^{H_x}\left(\frac{\tau}{\tau_c}\right)^{H_t}$ this will occur very rarely, since empirically, $\frac{\mu_{clim}}{\sigma_{anom}} \approx 80$, negative rain rates will clearly not be a problem at the largest scales $l=L_w$, $\tau=\tau_c$. However, if we take $\tau=\tau_w\approx 4$ days (the smallest time scale at which the model is valid) so that $\tau_c/\tau_w \approx 2000$, then assuming $H_t=-0.4$, $H_x=-0.2$ (Table I) we find that below a critical spatial resolution of $\approx$10 km the model implies frequent zeroes. Alternatively, as long as we stick to spatial scales larger than about 10 km and to time scales over macroweather time scales, the model will yield a positive raw rain rate and will be consistent with all the known statistics at scales $\tau > \tau_w$. Of course, if needed, negative raw rain rates can be truncated to zero, but this becomes problematic if the support (the nonzero part) becomes small.

4. Factorization and the statistical homogenization of climate data

In the calculation of drought indices (and in many other applications), one seeks to characterize whether the rain rate is low with respect to the "usual" local precipitation statistics; in other words, one seeks to homogenize precipitation series from stations that are climatologically different. A typical approach is to normalize the anomalies by dividing by the local standard deviation so as to obtain anomalies with essentially identical statistics (notice this implicitly assumes the statistical space-time factorization property).

To see how factorization works on our model, consider a single realization of the process, and a point $\underline{r}$ and then average the anomaly standard deviation over long times (i.e., to obtain a series at resolution τ_c)

$$\sigma_{R,\tau_c}(\underline{r}) = L_w^{-H_x}\sigma_{anom}\varphi_{c,l}(\underline{r}), \tag{41}$$

where we have used the result that the long time average over τ_c is approximately given by the ensemble average, and then used Eq. (23) to scale it to the low resolution τ_c. The "homogenized" process is thus obtained by normalizing the anomaly by its long term local variance

$$(R_{w,c,l,\tau}(\underline{r},t))_{\mathrm{hom}} = R_{w,c,l,\tau}(\underline{r},t)/\sigma_{R,\tau_c}(\underline{r}) \approx \tau_c^{-H_t}\varphi_{mw,l,\tau}(\underline{r},t), \tag{42}$$

which is a simple (statistically spatially homogeneous) space-time fGn process so that the inhomogeneity introduced by the climate process $\varphi_{c,l}$ has been removed. Using $\sigma_{R,\tau_c}(\underline{r})$, we have therefore obtained a "homogenized" process whose statistics are the same everywhere (this is a consequence of the space-time factorization which is exactly satisfied by the model). Note that this works as long as H_t is independent of spatial location; while this is apparently reasonable for precipitation, it is a poor approximation for the temperature field which involves spatially varying H_t. For other fields such as the latter, a more complex normalization is needed that takes into account the spatially varying H_t value.

The rainrate anomaly process $R(\underline{r},t)$ is the spatial extension of the basic SLIMM described in Lovejoy *et al.* (in press) and with temporal exponent H_t the same everywhere in space. It was motivated by the CEFIF model. It is approximate since the CEFIF is not exactly an fGn process, and because of the assumption that the spatial variability mostly derives from a low frequency multiplicative climate regime process (an admittedly *ad hoc* model choice). While we have assumed that H_t is constant in space, the relaxation of this assumption is important in application to macroweather forecasting and will be discussed elsewhere.

To summarize: the model for $R(\underline{r},t)$ describes macroweather precipitation variability as a fractional Gaussian noise process with spatially correlated amplitudes. The space-time statistics factor into separate spatial and temporal functions. Over periods over which φ_c can be considered independent of time (i.e., $\Delta t < \tau_c$, less than decadal, centennial scales), the spatial correlations are determined by $\varphi_{c,l}(\underline{r})$ which is a single realization of a multifractal climate process at resolution l. It takes into account the geographical variation which include notably the multifractal topography (Gagnon *et al.*, 2006). At each spatial location, the time series is a fGn process parameter H_t with standard deviation given by $\sigma_{R,\tau_c}(\underline{r})$ and depending on the temporal resolution via τ^{H_t}. In this way, the local statistics of the precipitation anomaly are determined in a multiplicative way by the climate process $\varphi_{c,l}(\underline{r})$. This justifies the simple expedient of normalizing (nondimensionalizing) the precipitation process at each spatial location by the standard deviation estimated from the time average at $\underline{r}$: $\sigma_{R,\tau_c}(\underline{r})$ (see Eq. (41)).

F. Empirically testing the statistical space-time factorization property

The space-time spectral density ("P_{xyt}") corresponding to the autocorrelation Eq. (36) is

$$\begin{aligned} P_{xyt}(\underline{k},\omega) &= F.T.(c_R(\underline{\Delta r},\Delta t)) \propto (F.T.(c_x(\underline{\Delta r})))(F.T.(c_t(\Delta t))) \\ &\approx P_{xy}(\underline{k})P_t(\omega) \approx |\underline{k}|^{-s_x}\omega^{-\beta_t}, \qquad (43) \\ s_x = \beta_x + d - 1; &\quad \beta_x = 1 + 2H_x - K(2); \quad \beta_t = 1 + 2H_t, \end{aligned}$$

which is expected to be valid for $\tau_w^{-1} < \omega < \tau_c^{-1}$ and where "F.T." means Fourier transform. This is the Wiener-Khinchin theorem relating the spectral density and the autocorrelation, $d = 2 =$ the dimension of x, y space.

In order to test this, we can simplify by considering zonal wavenumber frequency spectra. First, consider only the zonal direction (wavenumber k). If factorization holds, then $P_{xt}(k,\omega) = P_x(k)P_t(\omega)$ and the density $P_{xt}(k,\omega)$ will have iso-density contours parallel to the k, ω axes. Figure 7(a) shows the result for the 20CR reanalysis data, considering two latitudinal bands. Although the contours are noisy, they are fairly parallel to the axes hence they are compatible with statistical factorization. At the lowest 3 or so available frequencies (i.e., ≈30–40 year scales) factorization breaks down—the beginning of the climate regime—the vertically aligned contours near the centre of the plot. Elsewhere we show that this factorization behavior is reasonably well reproduced by GCM's although with somewhat different amplitudes and spatial scaling laws. A figure very similar to this, showing the factorization of space-time macroweather temperature spectra, was given in Lovejoy and Schertzer (2013), in section 10.3.

In order to investigate this further, we can directly check the constancy of the ratio $P_{xt}(k,\omega)/(P_x(k)P_t(\omega))$; the result is shown in Fig. 7(b) (see Fig. 9 for the corresponding plot for the CEFIF simulation). Over the range of k, ω shown, P_{xt} varies by a factor of $\approx 10^7$ while the ratio remains quite constant. To judge this, consider the various horizontal sections shown in the figure that are for k increasing by factors of two (bottom to top). We see that except for the lowest frequencies, the ratio is very constant, especially for the 30°–60°N band (right). For example, the variations about the bottom right line are only $\pm 20\%$.

We can also check the factorization directly in real space using joint space-time Haar fluctuations. In this case, for the RMS fluctuations we expect the joint $S(\Delta x,\Delta t)$ to be the product of a spatial function S_x and temporal function S_t

$$S(\Delta x,\Delta t) = S_x(\Delta x)S_t(\Delta t) \qquad (44)$$

(in the analyses, we actually use the zonal angle so that the symbol Δx is the longitude subtended by an arc on the earth's surface).

In order to facilitate the interpretation of the results, we can use the fact that in the time domain the fluctuations decrease with scale, hence if we simply average the anomalies over longer and longer time scales, the resulting averages are virtually the same as the corresponding Haar fluctuation (the differencing in Eq. (1) has little effect when $H < 0$). In space, we use the usual (spatial) Haar fluctuation of the temporally averaged data. For the GHCN data, this joint space-time analysis is shown in Fig. 8(a). We see not only that the curves are parallel for different amounts of averaging—the basic factorization prediction—but also that as we double the averaging time Δt the curves are roughly equally spaced; this demonstrates the scaling in time. In addition, the structure functions are more or less linear on the log-log plot so that there is also scaling in space. Overall we have Eq. (44) with

$$S_x(\Delta x) \approx \Delta x^{\xi_x(2)/2}; \quad S_t(\Delta t) \approx \Delta t^{H_t}, \qquad (45)$$

with $\xi_x(2)/2 \approx -0.3$, $H_t \approx -0.4$. Taking $K_x(2)/2 \approx C_1 \approx 0.1$ (see Eq. (6) and Table II) we have $H_x \approx -0.2$. Notice that since the temporal fluctuations are estimated by simply averaging the anomalies ($q = 1$), the spacing in the vertical allows us to directly infer H_t. In contrast, the RMS spatial fluctuations have exponent $\xi_x(2)/2$ which is a poor approximation to H_x due to the large spatial intermittency; it requires the correction $K_x(2)/2$ (see the estimates in Table II).

In Fig. 8(b), we show the analogous plot for the Smith product. Once again, the curves for different averaging times (top to bottom) are roughly equally spaced as predicted by Eq. (44); and the reference lines are spaced at factors $4^{-0.45}$ (corresponding to $H_t = -0.45$, with a factor 4 of temporal averaging, the same reference lines as the GHCN, Fig. 8(a)). However, up to 80° the slopes are very different: $\xi_x(2)/2 \approx +0.2$, hence $H_x \approx 0.1$, rather than $\xi_x(2)/2 \approx -0.3$ for the GHCN anomaly (Fig. 8(a)) although there is evidence for large scales that $\xi_x(2)/2 \approx -0.3$, i.e., the same as the GHCN exponent. In addition, the Smith anomaly also respects the factorization property, and the Smith $H_x \approx 0.1$ (Table I) is very close to those of the spatial satellite IR fields of the type that were used in its construction (with $H_x \approx 0.2$; see Lovejoy *et al.* (2009)). Finally, Fig. 8(c) shows the corresponding plot for the 20CR data. It is fairly close to the Smith data, although with slightly different parameters. In addition, the temporal scaling breaks down between about 10 and 20 years (128 and 256 months).

Also shown in Fig. 8(b) are the corresponding analyses for the raw rain rates averaged over 1, 2, 4,…, 512 months. We see that after about a year of temporal averaging the statistics have nearly converged to their long term values: the

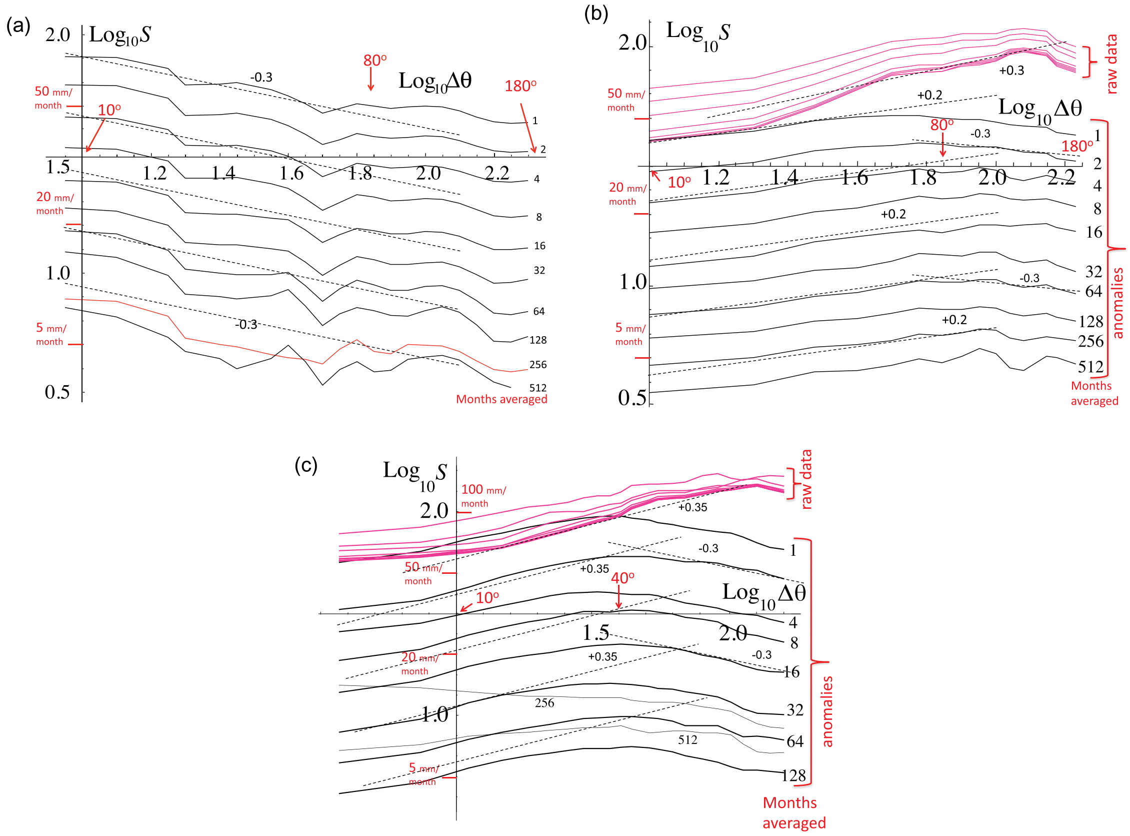

FIG. 8. (a) The $\log_{10}$ of the RMS structure functions of GHCN (anomalies) in the zonal (EW) direction (units: mm/month) for averaging times increasing from top to bottom by factors of 2 (in months). The longitudinal angle subtended is indicated: $\Delta\theta$ (i.e., an angular "lag" rather than a distance, the data were from latitudes between $\pm 45°$ so that the difference is not very important), this was indicated Δx in the text. One can see that up to the limit of the macroweather regime (in red—thick line—about 256 months, i.e., $\approx$20 years) the effect of averaging is essentially to systematically decrease the spatial structure function but without changing its shape (in this case, reasonably close to a power law fall-off). In addition, the dashed reference lines slopes $\xi_x(2)/2 \approx -0.3$, corresponding to $H_x \approx -0.2$ (since $C_1 \approx 0.1$, see Table II) are spaced so as to correspond to a factor $4^{-0.4}$, i.e., the theoretical spacing for two curves with a factor of 4 different in averaging time and with $H_t = -0.4$. This indicates that the joint structure function $S(\Delta x, \Delta t)$ satisfies Eq. (44), i.e., the predicted macroweather "factorization" property. (b) The RMS spatial structure function of the temporal analyses of the Smith product (units: mm/month). The bottom (black) is for the Smith anomalies, it is the analogue of the GHCN analysis (Fig. 8(a)), these approximate the joint space-time structure function $S(\Delta x, \Delta t)$. Once again, the curves for different averaging times (top to bottom) are roughly equally spaced as predicted by Eqs. (44) and (45): the reference lines are spaced at factors $4^{-0.4}$ as in Fig. 8(a) (corresponding to $H_t = -0.2$, and a factor 4 of temporal averaging, the same temporal scaling as the GHCN). However, the slope is very different: $\xi_x(2)/2 \approx +0.2$ (hence $H_x \approx 0.1$) rather than $\xi_x(2)/2 \approx -0.3$ for the GHCN anomaly, see Fig. 8(a), so that—at least for scales below 80°—the Smith anomaly (corresponding to the dashed lines on the left) has very different spatial statistics than the GHCN data. However, there is some indication (the far right reference lines with slopes $\xi_x(2)/2 = -0.3$ corresponding to $H_x \approx -0.1$) that the differences may not be important at large scales (in accord with the direct comparison in dLL). The top (pink) are the corresponding analyses for the raw rain rates averaged over 1, 2, 4,…, 512 months (top to bottom) and the top dashed line $\xi_x(2)/2 = 0.3$ is the estimate of the spatial climate exponent, see row 7, Table IV. (c) The same as (b) but for the 20CR data (1871–2012), and averaging data over all latitudes between $\pm 45°$. The dashed lines have the indicated slopes corresponding to $\xi_x(2)/2 = 0.35$ and the vertical spacing corresponds to $\xi_t(2)/2 = -0.45$ (every factor of 4 in time scale). These are consistent with the estimates in Tables I and II of $H_x = 0.2$, $C_{1x} = 0.15$ and $H_t = -0.42$, $C_{1t} = 0.03$ (taking $\alpha \approx 2$ in both cases). The anomalies show reasonable scaling with positive slopes up to about 50° after which there is some indication (the far right reference lines with slopes $\xi_x(2)/2 = -0.3$ corresponding to $H_x \approx -0.2$) that the differences with respect to the GHCN anomalies may not be important at large scales (in accord with the direct comparison in dLL). For the anomalies (black, bottom set), the temporal scaling is reasonably well respected up to 128 months, but for averaging over 256, 512 months, the scaling is badly broken, these lines are indicated "256," "512" are thin. The raw data (top, pink) are also reasonably scaling and correspond to averaging from one month to 512 months, roughly with spatial exponent $\xi_x(2)/2 = 0.35$, $H_x = 0.2$, see Table IV, row 7.

spatial variability of annual averaged precipitation is nearly the same as for centennial averages.

Note that, when performing averaging on anomalies (the bottom curves), as explained above, since $H_t < 0$, the result is close to the corresponding Haar fluctuation. However, this is not true when averaging the raw data so that the top curves are not joint space-time Haar fluctuations, but simply spatial Haar fluctuations at various temporal resolutions. In fact, there is a difference in the anomalies and raw statistics in space, but not in time (see dLL for details), hence the different exponent estimates in Tables III and IV.

IV. DISCUSSION AND CONCLUSIONS

Over the last decades, there have been numerous scaling analyses of precipitation and other atmospheric fields, so that several fundamental aspects of atmospheric dynamics have been clarified. For example, over time scale ranges from weather scales up to $\approx$100 kyrs (ice-age scales), there is an intermediate macroweather regime which is, in between the familiar weather and climate, roughly spanning the range of 10 days to 30 years (industrial, 100 years or longer, preindustrial). The three regimes alternate in their basic characters. In the weather and climate regimes, average fluctuations tend to grow with scale ($H > 0$), they appear unstable. In contrast, in the macroweather regime they decrease with scale ($H < 0$), they appear stable. A recent analysis (Lovejoy, 2014) finds that this alternation continues through two larger scale (macroclimate and megaclimate) regimes out to time scales of over 500 Myrs.

Scaling analyses of macroweather precipitation have mostly used monthly station data and the analyses have often used difficult to interpret statistical methods (such as the Detrended Fluctuation Analysis technique), and this has hindered the emergence of a clear overall picture of annual, decadal, and centennial scale precipitation variability. Surprisingly, with the exception of dLL, there have been no attempts to characterize the spatial macroweather variability nor—the focus of this paper—the more fundamental joint space-time macroweather variability needed to construct space-time macroweather models (in contrast, there have been many spatial scaling analyses of precipitation in the weather regime).

Due to the extreme precipitation variability (high multifractal intermittency), the statistics have strongly nonclassical behaviors. An important (near) exception is the temporal macroweather variability that has a small C_1 (this characterizes the intermittency near the mean) and is therefore not too far from being quasi-Gaussian, see Table II (although the extremes are apparently quite non-Gaussian: power laws). Indeed of all the usual atmospheric fields, both at weather and macroweather scales, precipitation has the largest C_1. This intermittency, combined with the long range statistical dependencies implied by the scaling has seriously hampered conventional attempts (such as the decadal trend estimates in the IPCC AR4) to demonstrate the existence of anthropogenic increases in precipitation, and this in spite of simple and direct physical, theoretical connections between increased temperatures and increased precipitation. Since the conventional station precipitation series such as the GHCN product are for land only, in addition to this product, we also studied the globally complete 20CR product (Compo *et al.*, 2011) and the satellite based "Smith" (Smith *et al.*, 2012) global precipitation product.

The global space-time scaling up to planetary scales and lifetimes of planetary structures (Fig. 3) allows the atmosphere to be modeled up to those scales using the stochastic Fractionally Integrated Flux (FIF) model. Motivated by its success at weather scales ($\tau < \tau_w$), it was extended to much longer time scales: the EFIF model. The long time properties of EFIF ($\tau > \tau_w$) (some of which are worked out in Appendix 10A of Lovejoy and Schertzer (2013)) are that one generically obtains temporal macroweather exponents H in the range $-0.5 < H_t < 0$ (especially, in the range $-0.4 < H_t < -0.2$). As we explore in the Appendix, the EFIF model outlined in Sec. III C also predicts that a statistical space-time macroweather factorization property should approximately hold, a property that was verified on temperature data in Lovejoy and Schertzer (2013) and that is routinely used in practical climatology when series are "homogenized" by using their local variances. From a physical point of view, the main problem with the EFIF model is that it predicts fairly smooth spatial macroweather fields; whereas in reality they are much more variable (intermittent) in space than in time. This corresponds to the existence of different climate "zones" that modulate the local weather and macroweather. Respecting the space-time factorization and the multiplicative structure of the model, it was proposed that a more realistic model would result if a very low frequency multifractal climate process modulated the weather–macroweather EFIF model. The result weather–climate process is called the Climate EFIF model, CEFIF. It was numerically investigated in Sec. III D and—within the limitations of the numerics and the data—was found to explain 8 or more spatial and temporal exponents even though the model only had 4 exponents.

In order to get good macroweather statistics with the CEFIF model, the weather regime must be simulated and then averaged out, this makes it numerically cumbersome. In addition, the theoretical macroweather properties of the model are difficult to handle and analyze. We therefore developed another purely macroweather model (with ready extensions to the lower frequency climate regime). This was based on a recent paper (Lovejoy *et al.*, in press) showing how individual macroweather time series (using the example of the mean global scale temperature) can be modeled using fractional Gaussian noise (fGn). fGn is the simplest relevant scaling process with $H_t < 0$ (its order one integral is the more familiar fractional Brownian motion); the resulting model was called SLIMM. In Sec. III E, we therefore derived the space-time SLIMM model with spatially uniform H_t notably respecting space-time factorization. This space-time SLIMM involves temporal fGn processes at each spatial location with amplitudes spatially correlated according to a very low frequency spatial multifractal climate process; the prediction problem has therefore been solved for the SLIMM model. SLIMM is for anomalies; to extend the model to the raw rain rates we added a climate process proportional to the same process that modulates the anomalies from one location to another. Empirically and theoretically, this was shown to be realistic over the entire macroweather range. In this simplest version of the model, the long term average (climate) rainrates have exactly the same spatial variability as the standard deviations of the rainrate anomalies.

In the spectral domain, the space-time factorization implies that the spectral density approximately verifies $P_{xyt}(k_x,k_y,\omega) = P_{xy}(k_x,k_y)\ P_t(\omega)$, a property that we demonstrated on the 20CR precipitation data. For simplicity considering only latitudinal variations (wavenumbers k_x), we found that over ranges of k_x, ω where $P_{xt}(k_x,\omega)$ varies by a factor 10^7, the ratio $P_{xt}(k_x,\omega)/(P_x(k_x)\ P_t(\omega))$ varies by typically $\pm 20\%$. In real space, factorization predicts that joint structure functions should also decompose into separate spatial and temporal factors, a property that we confirmed on all three datasets. Physically, the interpretation is that spatial variations in macroweather statistics are controlled by different "climatic zones" which modulate the otherwise qualitatively similar (scaling) temporal variability. This property is already implicitly widely used, for example, when local climate states are "homogenized" by nondimensionalizing their statistics (including probabilities) by using standard deviations of local anomaly fluctuations.

The work described here clarifying and modeling space-time macroweather precipitation variability is a necessary step not only for understanding macroweather precipitation and the limitations of the corresponding precipitation products but is also necessary in the stochastic forecasting of macroweather fields. The potential of such forecasts is great since the temporal scaling implies that in macroweather there are strong long range memories that can potentially be exploited. This promises to overcome many of the limitations of conventional (deterministic) GCM climate forecasts.

ACKNOWLEDGMENTS

We thank A. Bussy for help with the analysis of the Smith product. This work was unfunded; there are no conflicts of interest.

APPENDIX: FACTORIZATION IN THE EFIF MODEL

1. The one point weather and macroweather statistics

a. Weather regime

In chap. 10, Lovejoy and Schertzer (2013) gave a mostly intuitive argument for factorization of the space-time statistical properties of macroweather. In this Appendix, we give the argument in more mathematical detail.

First, recall the properties of the (unit amplitude, extremal) Levy noise $\gamma(\underline{r},t)$ index $0 \le \alpha \le 2$

$$K_\gamma(q) = \log\langle e^{q\gamma}\rangle = \frac{q^\alpha}{\alpha-1}; \quad 0 \le \alpha \le 2, \tag{A1}$$

where K_γ is the second (Laplacian) characteristic function of γ; $\alpha = 2$ is the Gaussian limit used in SLIMM, $\alpha < 2$ are the infinite variance Levy cases, $\underline{r} = (x,y)$ is the horizontal, and t is time. When $\alpha < 2$, the γ must be maximally asymmetric so that only the negative side of the γ distribution has a power law probability tail (hence the adjective "extremal"), i.e., it has a probability density $p(\gamma) \approx |\gamma|^{-\alpha-1}; \quad \gamma \ll -1$.

A basic property of second characteristic functions (SCF) is that for sums of independent identically distributed random variables, they are additive

$$\Gamma(\underline{r},t) = N\int g(\underline{r}-\underline{r}', t-t')\gamma(\underline{r}',t')d^2\underline{r}'dt';$$
$$K_\Gamma(q) = \log\langle e^{q\Gamma}\rangle = \frac{N^\alpha q^\alpha}{\alpha-1}\int g(\underline{r}',t')^\alpha d^2\underline{r}'dt', \tag{A2}$$

where $g \ge 0$ and N is a normalization factor introduced for convenience. If we now take

$$g(\underline{R}) = \Theta(t)R^{-d/\alpha}; \quad \underline{R} = (\underline{r},t); \quad R = |\underline{R}| = (r^2+t^2)^{1/2};$$
$$\underline{r} = (x,y); \quad r = |\underline{r}| = (x^2+y^2)^{1/2}, \tag{A3}$$

where $d = 3$ (the dimension of (x,y,t) space) and Θ is the Heaviside function needed for causality ($\Theta(t) = 1$, $t \ge 0$; $\Theta(t) = 0$, $t < 0$).

Applying the above to the weather regime (see Fig. 5(b) for the region of integration)

$$K_{\Gamma,w}(q) \approx \frac{N^\alpha q^\alpha}{\alpha-1}\int_{\Lambda_w^{-1}}^{1}\int_{\Omega_d}\left(R^{-3/\alpha}\right)^\alpha R^2 dR d\Omega = \frac{N^\alpha q^\alpha}{\alpha-1}\Omega_d \log\Lambda_w, \tag{A4}$$

where dΩ is an element of solid angle and Ω_d is the solid angle of a half sphere ($=2\pi$; the half is due to the Heaviside function). The volume of integration has been taken to be the region between concentric (half) spheres with radii $\Lambda_w{}^{-1}$ and 1 (with $t \ge 0$), which is approximately the (cylindrical) region indicated in Fig. 5(b) for the weather regime. We now obtain

$$\langle\varphi_{\Lambda_w}^q\rangle = \langle e^{q\Gamma_w}\rangle = e^{K_w(q)} = \Lambda_w^{\frac{C_1}{\alpha-1}q^\alpha}; \quad C_1 = N^\alpha\Omega_d\,. \tag{A5}$$

The reason for the choice of exponent $-d/\alpha$ in Eq. (A3) is now clear; it leads to the required log divergence of $K_{\Gamma,w}$ with cascade scale ratio Λ_w (Eq. (A4)). To obtain the qth moment of the universal multifractal (Eqs. (9) and (10)), we need only to normalize the process

$$\langle\varphi_{\Lambda_w}^q\rangle \to \langle\varphi_{\Lambda_w}^q\rangle / \langle\varphi_{\Lambda_w}\rangle^q;$$
$$K_w(q) \to K_w(q) - qK_w(1) = \frac{C_1}{\alpha-1}(q^\alpha - q). \tag{A6}$$

b. Macroweather regime

We have calculated the statistical properties of the "bare" weather regime cascade, i.e., the properties at the highest resolution of a cascade developed over a scale range Λ_w and then stopped. In practice, we are usually interested in the "dressed" properties, i.e., the statistics of a cascade developed over a wide range but then averaged to an intermediate scale ratio $1 < \lambda < \Lambda_w$. For these multiscaling, multifractal cascades the only difference between the bare and dressed properties is that the latter generally have stronger extremes; divergence of statistical moments high order than a critical value q_D (for precipitation $q_D \approx 3$ see Table 5.1b of Lovejoy and Schertzer (2013) and dLL for weather and macroweather, respectively). However, in the macroweather regime, the bare and dressed properties will be quite different. Nevertheless, if we average ("dress") by temporal averaging, this will not affect the factorization property that we will now investigate.

Consider the macroweather term with $d = 3$, the SCF is

$$K_{\Gamma,mw}(q) = \frac{C_1(2\pi)^{-1}q^\alpha}{\alpha-1}\int_0^{2\pi}\int_{\Lambda_w^{-1}}^{1}\int_1^{\Lambda_c}(r^2+t^2)^{-3/2} r\,dr\,d\theta\,dt$$
$$\approx \frac{C_1 q^\alpha}{\alpha-1}\log\left[\left(\frac{1+\sqrt{2}}{2}\right)\left(1-(2\Lambda_c)^{-2}+O(\Lambda_c)^{-4}\right)\right], \tag{A7}$$

where $\Lambda_c = \tau_c/\tau_w$ is the scale ratio of the macroweather part of the cascade (we have put $\Lambda_w^{-1} = 0$, it is unimportant here). For the (unnormalized) flux, we have

$$\langle \varphi_{mw}^q \rangle = e^{K_{mw}(q)} \approx \left[\left(\frac{1+\sqrt{2}}{2} \right) \left(1 - (2\Lambda_c)^{-2} \right) \right]^{\frac{C_1}{\alpha-1} q^\alpha}. \quad \text{(A8)}$$

We therefore see that for large Λ_c, the moments asymptote (according to a power law) to the value

$$\langle \varphi_{mw}^q \rangle \approx \left(\frac{1+\sqrt{2}}{2} \right)^{\frac{C_1}{\alpha-1} q^\alpha}. \quad \text{(A9)}$$

This type of power law convergence to a constant is the hallmark of $H < 0$ processes.

2. The two point statistics and statistical space-time macroweather factorization

The above results are for the one-point statistics of a process developed over various ranges of scale (Λ_w for the weather process and Λ_c for the macroweather component). If we want to understand the internal structure, we need to consider two point (or higher order multipoint) statistics such as the autocorrelations or its Fourier transform, the spectrum. In particular, we wish to show that the autocorrelation (at least approximately) factorizes into separate spatial and temporal functions.

To calculate the autocorrelation function, we first evaluate the lagged product

$$\begin{aligned} (\varphi(\underline{R}' - \underline{\Delta R})\varphi(\underline{R}')) &= e^{(\Gamma(\underline{R}' - \underline{\Delta R}) + \Gamma(\underline{R}'))} \\ &= e^{C_1^{1/\alpha} \int_M (g(\underline{R}' - \underline{\Delta R} - \underline{R}) + g(\underline{R}' - R))\gamma(\underline{R}) d^d \underline{R}}; \\ M &= \{\Lambda_w^{-1} \le |\underline{r}| \le 1, 1 \le t \le \Lambda_c\}, \quad \text{(A10)} \end{aligned}$$

where $\underline{R} = (\underline{r}, t) = (x, y, t)$ and M is the macroweather region of integration (see Fig. 5(b)), note that taking $t > 0$ accounts for the Heaviside function, the causality constraint (we have put $N = 1$, it is unimportant here). We can now calculate the SCF of the autocorrelation by taking qth powers and statistical averaging

$$\log \langle (\varphi(\underline{R} - \underline{\Delta R})\varphi(\underline{R}))^q \rangle = \frac{q^\alpha}{\alpha - 1} C_1 S(\underline{\Delta R}), \quad \text{(A11)}$$

with

$$S(\underline{\Delta R}) = \int_M (g(\underline{R}' - \underline{\Delta R} - \underline{R}) + g(\underline{R}' - \underline{R}))^\alpha d^d \underline{R}, \quad \text{(A12)}$$

where $S(\underline{\Delta R})$ is the spatial part of the SCF (not to be confused with the structure function). Since the statistics are translationally invariant (statistical homogeneous), R' does not appear. Using symmetries, we obtain

$$S(\underline{\Delta R}) = \int_M (g(\underline{R} - \underline{\Delta R}) + g(\underline{R}))^\alpha d^d \underline{R}, \quad \text{(A13)}$$

M is the macroweather integration volume (above) and $d = 3$ here (for (x,y,t) space see Lovejoy and Schertzer (2013), Appendix 5B).

Statistical space-time factorization will follow if for some functions $F(\Delta \underline{r})$ and $G(\Delta t)$

$$\langle (\varphi(\underline{R} - \underline{\Delta R})\varphi(\underline{R})) \rangle = e^{F(\underline{\Delta r})} e^{G(\Delta t)}, \quad \text{(A14)}$$

i.e., if

$$S(\underline{\Delta R}) \approx F(\underline{\Delta r}) + G(\Delta t). \quad \text{(A15)}$$

Therefore, if we expand $S(\underline{\Delta R})$ in a series in Δr, Δt, there should be no space-time cross-terms such as $|\underline{\Delta r}|\Delta t$. Isotropic terms such as $|\underline{\Delta R}|^p = (|\underline{\Delta r}|^2 + \Delta t^2)^{p/2}$ will break the factorization property but only weakly since in the macroweather regime, $\Delta t > 1 > |\underline{\Delta r}|$; in the large Δt limit, factorization will be respected by such terms.

Using $g(\underline{R}) = |\underline{R}|^{-d/\alpha}$ there are two regions of integration to consider:

Region 1: $|\underline{\Delta R}| < |\underline{R}|$

Considering just the integrand, repeated use of the binomial expansion, keeping only the leading terms yields

$$\begin{aligned} &(g(\underline{R} - \underline{\Delta R}) + g(\underline{R}))^\alpha \\ &\quad = \left(|\underline{R} - \underline{\Delta R}|^{-d/\alpha} + |\underline{R}|^{-d/\alpha} \right)^\alpha \\ &\quad \approx 2^\alpha |\underline{R}|^{-d} \left(1 + \frac{d}{4} u + \frac{d}{8} \left(\frac{d}{2\alpha} + 1 \right) u^2 + \cdots \right); \\ &u = -2 \frac{\underline{R} \cdot \underline{\Delta R}}{|\underline{R}|^2} + \left(\frac{|\underline{\Delta R}|}{|\underline{R}|} \right)^2. \quad \text{(A16)} \end{aligned}$$

Note that although the binomial expansions involved are only valid for $u < 1$, the series is convergent for $|\underline{\Delta R}|/|\underline{R}| < 1$ as can be shown by bounding it in the extreme cases where $\underline{\Delta R}$ is parallel and antiparallel to $\underline{R}$.

Let us now consider the significance of the above expansion term by term. The first term on the right ($|\underline{R}|^{-d}$), when integrated over the integration region M will yield a constant, that (after exponentiation) will contribute a constant factor to the autocorrelation; we are interested in the $\underline{\Delta r}$ and Δt behaviours, these are in the higher order terms. From the expansion, we see that we need to consider the behaviour of powers of $\underline{R} \cdot \underline{\Delta R} = \underline{r} \cdot \underline{\Delta r} + t\Delta t$ and of $|\underline{\Delta R}|^2 = |\underline{\Delta r}|^2 + |\Delta t|^2$, and recall that we integrate them over the region M that has cylindrical symmetry about the t axis. Because of this symmetry, any integrals of odd powers of $\underline{r} \cdot \underline{\Delta r}$ will vanish. Therefore, the $\underline{R} \cdot \underline{\Delta R}$ term will contribute only a Δt dependence. As for the $|\underline{\Delta R}|^2$ term (of order $(|\underline{\Delta R}|/|\underline{R}|)^2$), it contributes to the $\underline{\Delta r}$ dependence but there are no cross terms so that it respects factorization. Considering next the u^2 term, we see that the term $(\underline{R} \cdot \underline{\Delta R})^2 = (\underline{r} \cdot \underline{\Delta r})^2 + (t\Delta t)^2 + 2(\underline{r} \cdot \underline{\Delta r})(t\Delta t)$ will contribute to both a $\underline{\Delta r}$ and Δt dependency, but the cross term again vanishes by symmetry. However (finally!), the $|\underline{\Delta R}|^4 = |\underline{\Delta r}|^4 + 2|\underline{\Delta r}|^2 \Delta t^2 + \Delta t^4$ term (fourth order in $(|\underline{\Delta R}|/|\underline{R}|)$) does contribute a factorization symmetry breaking term $2|\underline{\Delta r}|^2 \Delta t^2$. Actually, if we consider the series up to u^3, then we find a term proportional to $(\underline{R} \cdot \underline{\Delta R})^3 = (\underline{r} \cdot \underline{\Delta r})^3 + 3(\underline{r} \cdot \underline{\Delta r})^2 (t\Delta t) + 3(\underline{r} \cdot \underline{\Delta r})(t\Delta t)^2 + (t\Delta t)^3$ (third order in

$(|\underline{\Delta R}|/|\underline{R}|)$) that has a factorization symmetry breaking term $3(\underline{r}\cdot\underline{\Delta r})^2(t\Delta t)$ (again, the term $3(\underline{r}\cdot\underline{\Delta r})(t\Delta t)^2$ vanishes by the circular symmetry of the $\underline{r}$ integration).

To summarize, when $|\underline{R}| > |\underline{\Delta R}|$ the zeroth order term leads to a constant, the first order term to the Δt dependence, the 2nd order to Δt and $\underline{\Delta r}$ dependence so that the first cross term that breaks the factorization symmetry is the third order term.

Region 2: $|\underline{\Delta R}| > |\underline{R}|$

In this case, we can follow the approach of Lovejoy and Schertzer (2010b) and introduce the ratio v

$$v = \left(\frac{|\underline{R}| - |\underline{\Delta R}|}{|\underline{R}|}\right)^2 = |\underline{\Delta R}|^2(1+w);$$
$$w = -\frac{2\underline{R}\cdot\underline{\Delta R}}{|\underline{\Delta R}|^2} + \frac{|\underline{R}|^2}{|\underline{\Delta R}|^2}. \tag{A17}$$

With this

$$(|\underline{R}-\underline{\Delta R}|^{-d/\alpha} + |\underline{R}|^{-d/\alpha})^\alpha = \begin{array}{l} |\underline{R}|^{-d}(1+v^{-d/\alpha})^\alpha; \quad v>1; \quad |\underline{R}-\underline{\Delta R}| > |\underline{R}| \\ |\underline{R}-\underline{\Delta R}|^{-d}(1+v^{d/\alpha})^\alpha; \quad v<1; \quad |\underline{R}-\underline{\Delta R}| < |\underline{R}| \end{array}, \tag{A18}$$

so that we can make the following Binomial expansions for each case separately ($v>1$, $v<1$).

Case (a) $v > 1$; $|\underline{R}-\underline{\Delta R}| > |\underline{R}|$**:**

$$\underline{R}^{-d}\left(1+v^{-d/\alpha}\right)^\alpha = |\underline{R}|^{-d}\left(1+\alpha v^{-d/(2\alpha)} + \frac{\alpha(\alpha+1)}{2}v^{-d/\alpha} + \cdots\right), \tag{A19}$$

with the nth term in the expansion given by the series

$$\left(v^{-d/(2\alpha)}\right)^n = |\underline{\Delta R}|^{-nd/\alpha}\left(1-\left(\frac{nd}{2\alpha}\right)w + \frac{1}{2}\left(\frac{nd}{2\alpha}\right)\left(\frac{nd}{2\alpha}-1\right)w^2 + \cdots\right), \tag{A20}$$

which is effectively an expansion in terms of $\frac{2\underline{R}\cdot\underline{\Delta R}}{|\underline{\Delta R}|^2}$ (recall in this region of integration $|\underline{R}| < |\underline{\Delta R}|$).

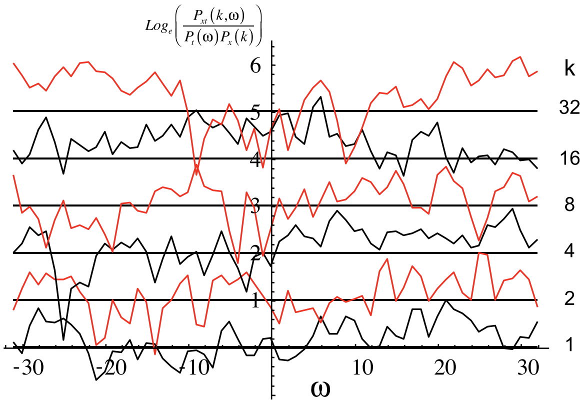

FIG. 9. This is the figure analogous to Fig. 7(b) but for the numerical weather, macroweather EFIF simulation (on a $2^7\times 2^7\times 2^{12}$ (x,y,t) grid) described in Sec. III F with each wavenumber curve displaced by a factor e (not $e^{0.5}$ as in Fig. 7(b)) in the vertical for clarity. The simulation was temporally averaged over range of 2^6 in time (essentially the weather regime which is 2^7 pixels), so that it tests the constancy of the dressed macroweather statistics over the (simulated) range of frequencies (10 days)$^{-1}$ to (320 days)$^{-1}$ and wavenumbers (20 000/32 km)$^{-1}$ to (20 000 km)$^{-1}$. The largest systematic deviations (at large k) are of the order a factor e, whereas the actual range of the joint spectrum is a factor ≈200 over this range of frequencies and wavenumbers.

First, consider the zeroth order terms $|\underline{\Delta R}|^{-nd/\alpha} = (|\underline{\Delta r}|^2 + \Delta t^2)^{-nd/\alpha}$. This will in fact break the factorization, but as mentioned above, only weakly because $\Delta t > 1 > \Delta r$. By cylindrical symmetry, after integration, the first order term $\frac{\underline{R}\cdot\underline{\Delta R}}{|\underline{\Delta R}|^2} = \frac{\underline{r}\cdot\underline{\Delta r}+t\Delta t}{|\underline{\Delta r}|^2+\Delta t^2}$ will give only a contribution $\frac{\Delta t}{|\underline{\Delta r}|^2+\Delta t^2} \approx \Delta t^{-1}$ to the autocorrelation. The second order term $|\underline{\Delta R}|^{-2} = (|\underline{\Delta r}|^2 + \Delta t^2)^{-1} \approx \Delta t^{-2}$ will likewise only weakly break the factorization symmetry (when Δt is small, $\underline{\Delta r}$ large). Continuing, we find that we again need to consider third order terms in $|\underline{R}|/|\underline{\Delta R}|$ before the numerator displays a factorization breaking term.

Case b) $v < 1$; $|\underline{R}-\underline{\Delta R}| < |\underline{R}|$

In this case, we have

$$|\underline{R}-\underline{\Delta R}|^{-d}\left(1+v^{d/\alpha}\right)^\alpha = |\underline{\Delta R}|^{-d}(1+w)^{-d/2}\left(1+v^{d/\alpha}\right)^\alpha \times\left(1+\alpha v^{d/(2\alpha)} + \frac{\alpha(\alpha+1)}{2}v^{d/\alpha} + \cdots\right). \tag{A21}$$

The analysis is thus essentially the same as above for the series in v (but with d replaced by $-d$) and with the extra term: $(1+w)^{-d/2}$.

In conclusion, $S(\underline{\Delta R})$ has an expansion in separate powers of Δt and $\underline{\Delta r}$, with no $\underline{\Delta r}\Delta t$ terms before third order. The only exception is when Δt is near the macroweather minimum ($\Delta t \approx 1$) and $\underline{\Delta r}$, near the spatial maximum ($\Delta r \approx 1$). This means that that the autocorrelation function factors into separate spatial and temporal functions to the same order. Figure 9 confirms this on the dressed numerical EFIF simulations described in Sec. III D).

Biagini, F., Hu, Y., Øksendal, B., and Zhang, T., *Stochastic Calculus for Fractional Brownian Motion and Applications* (Springer-Verlag, London, 2008).

Bunde, A., Eichner, J. F., Kantelhardt, J. W., and Havlin, S., "Long-term memory: A natural mechanism for the clustering of extreme events and anomalous residual times in climate records," Phys. Rev. Lett. **94**, 048701 (2005).

Bunde, A., Büntgen, U., Ludescher, J., Luterbacher, J., and von Storch, H., "Is there memory in precipitation?," Nat. Clim. Change **3**, 174–175 (2013).

Compo, G. P., *et al.*, "The twentieth century reanalysis project," Q. J. R. Meteorolog. Soc. **137**, 1–28 (2011).

de Lima, M. I. P., "Multifractals and the temporal structure of rainfall," Ph.D. thesis (Wageningen Agricultural University, Wageningen, The Netherlands, 1998), 225 pp.

de Lima, M. I. P. and de Lima, J. L. M. P., "Investigating the multifractality of point precipitation in the Madeira archipelago," Nonlinear Processes Geophys. **16**, 299–311 (2009).

de Lima, M. I. P. and Lovejoy, S., "Macroweather precipitation variability up to global and centennial scales," Water Resour. Res. (submitted).

de Montera, L., Barthès, L., Mallet, C., and Golé, P., "Rain universal multifractal parameters revisited with dual-beam spectropluviometer measurements," J. Hydrometeorol. **10**, 493–506 (2009).

Douglas, E. M. and Barros, A. P., "Probable maximum precipitation estimation using multifractals: Applications to the eastern United States," J. Hydrometeorol. **4**, 1012–1024 (2003).

Gagnon, J. S., Lovejoy, S., and Schertzer, D., "Multifractal earth topography," Nonlinear Processes Geophys. **13**, 541–570 (2006).

Garcia-Marin, A. P., Jimenez-Hornero, F. J., and Ayuso-Munoz, J. L., "Universal multifractal description of an hourly rainfall time series from a location in southern Spain," Atmosfera **21**, 347–355 (2008).

Gires, A., Tchiguirinskaia, I., Schertzer, D., and Lovejoy, S., "Development and analysis of a model to represent the zero rainfall in a universal multifractal framework," Nonlinear Processes Geophys. **20**, 343–356 (2013).

Hoang, C. T., Tchiguirinskaia, I., Schertzer, D., Arnaud, P., Lavabre, J., and Lovejoy, S., "Assessing the high frequency quality of long rainfall series," J. Hydrol. **438–439**, 39–51 (2012).

Kalnay, E., *Atmospheric Modelling, Data Assimilation and Predictability* (Cambridge University Press, Cambridge, 2003).

Kantelhardt, J. W., Koscielny-Bunde, E., Rybski, D., Braun, P., Bunde, A., and Havlin, S., "Long-term persistence and multifractality of precipitation and river runoff record," J. Geophys. Res. **111**, 2156–2202, doi:10.1029/2005JD005881 (2006).

Kolesnikov, V. N. and Monin, A. S., "Spectra of meteorological field fluctuations," Izv., Atmos. Oceanic Phys. **1**, 653–669 (1965).

Ladoy, P., Lovejoy, S., and Schertzer, D., "Extreme Variability of climatological data: Scaling and Intermittency," in *Non-linear Variability in Geophysics: Scaling and Fractals* edited by D. Schertzer and S. Lovejoy (Kluwer, 1991), pp. 241–250.

Lawrimore, J. H., Menne, M. J., Gleason, B. E., Williams, C. N., Wuertz, D. B., Vose, R. S., and Rennie, J., "An overview of the Global Historical Climatology Network monthly mean temperature data set, version 3," J. Geophys. Res. **116**, D19121, doi:10.1029/2011JD016187 (2011).

Lovejoy, S., "A voyage through scales, a missing quadrillion and why the climate is not what ou expect," Clim. Dyn. **44**, 3187–3210 (2014).

Lovejoy, S. and Schertzer, D., "Scale invariance in climatological temperatures and the local spectral plateau," Ann. Geophys. **4B**, 401–410 (1986).

Lovejoy, S. and Schertzer, D., "On the simulation of continuous in scale universal multifractals. II. Space-time processes and finite size corrections," Comput. Geosci. **36**, 1404–1413 (2010a).

Lovejoy, S. and Schertzer, D., "On the simulation of continuous in scale universal multifractals. I. Spatially continuous processes," Comput. Geosci. **36**, 1393–1403 (2010b).

Lovejoy, S. and Schertzer, D., "Towards a new synthesis for atmospheric dynamics: space-time cascades," Atmos. Res. **96**, 1–52 (2010c).

Lovejoy, S. and Schertzer, D., "Low frequency weather and the emergence of the Climate," in *Extreme Events and Natural Hazards: The Complexity Perspective*, Geophysical Monograph Series, edited by A. S. Sharma, A. Bunde, D. N. Baker, and V. P. Dimri (AGU, 2012a), pp. 231–254.

Lovejoy, S. and Schertzer, D., "Haar wavelets, fluctuations and structure functions: convenient choices for geophysics," Nonlinear Proc. Geophys. **19**, 513–527 (2012b).

Lovejoy, S. and Schertzer, D., *The Weather and Climate: Emergent Laws and Multifractal Cascades* (Cambridge University Press, Cambridge, 2013), 496 pp.

Lovejoy, S., Schertzer, D., and Allaire, V., "The remarkable wide range scaling of TRMM precipitation," Atmos. Res. **90**, 10–32 (2008).

Lovejoy, S., Schertzer, D., Allaire, V., Bourgeois, T., King, S., Pinel, J., and Stolle, J., "Atmospheric complexity or scale by scale simplicity?," Geophys. Res. Lett. **36**, L01801, doi:10.1029/2008GL035863 (2009).

Lovejoy, S., Pinel, J., and Schertzer, D., "The Global space-time Cascade structure of precipitation: Satellites, gridded gauges and reanalyses," Adv. Water Res. **45**, 37–50 (2012).

Lovejoy, S., Schertzer, D., and Tchiguirinskaia, I., "Further (monofractal) limitations of climactograms," Hydrol. Earth Syst. Sci. Discuss. **10**, C3086–C3090 (2013).

Lovejoy, S., Muller, J. P., and Boisvert, J. P., "On Mars too, expect macroweather," Geophys. Res. Lett. **41**, 7694–7700, doi:10.1002/2014GL061861 (2014).

Lovejoy, S., del Rio Amador, L., and Hébert, R., "The Scaling LInear Macroweather Model (SLIMM): Using scaling to forecast global scale macroweather from months to decades," Earth Syst. Dynam. Discuss. **6**, 489–545 (2015).

Mandapaka, P. V., Villarini, G., Seo, B.-C., and Krajewski, W. F., "Effect of radar-rainfall uncertainties on the spatial characterization of rainfall events," J. Geophys. Res. **115**, D17110, doi:10.1029/2009JD013366 (2010).

Marsan, D., Schertzer, D., and Lovejoy, S., "Causal space-time multifractal processes: Predictability and forecasting of rain fields," J. Geophy. Res. **101**(D21), 26333–26346 (1996).

Panofsky, H. A., "The spectrum of temperature," J. Radio Sci. **4**, 1143–1146 (1969).

Pathirana, A., Herath, S., and Yamada, T., "Estimating rainfall distributions at high temporal resolutions using a multifractal model," Hydrol. Earth Syst. Sci. **7**, 668–679 (2003).

Pinel, J. and S. Lovejoy, "Atmospheric waves as scaling, turbulent phenomena," Atmos. Chem. Phys. **14**, 3195–3210 (2014).

Pinel, J., Lovejoy, S., and Schertzer, D., "The horizontal space-time scaling and cascade structure of the atmosphere and satellite radiances," Atmos. Res. **140–141**, 95–114 (2014).

Rysman, J.-F., Verrier, S., Lemaître, Y., and Moreau, E., "Space-time variability of the rainfall over the western Mediterranean region: A statistical analysis," J. Geophys. Res. Atmos. **118**, 8448–8459 (2013).

Schertzer, D. and Lovejoy, S., "Physical modeling and analysis of rain and clouds by anisotropic scaling of multiplicative processes," J. Geophys. Res. **92**, 9693–9714, doi:10.1029/JD092iD08p09693 (1987).

Smith, T. M., Reynolds, R. W., Peterson, T. C., and Lawrimore, J., "Improvements to NOAA's historical merged land-ocean surface temperature analysis (1880–2006)," J. Clim. **21**, 2283–2293 (2008).

Smith, T. M., Arkin, P. A., Ren, L., and Shen, S. S. P., "Improved reconstruction of global precipitation since 1900," J. Atmos. Oceanic Technol. **29**, 1505–1517 (2012).

Sun, X. and Barros, A. P., "An evaluation of the statistics of rainfall extremes in rain gauge observations and satellite-based and reanalysis products using Universal Multifractals," J. Hydrometeorol. **11**, 388–404 (2010).

Tessier, Y., Lovejoy, S., Hubert, P., Schertzer, D., and Pecknold, S., "Multifractal analysis and modeling of Rainfall and river flows and scaling, causal transfer functions," J. Geophy. Res. **101**, 26427–26440 (1996).

Vallis, G., "Mechanisms of climate variability from years to decades," in *Stochastic Physics and Climate Modelling* edited by P. W. T. Palmer (Cambridge University Press, Cambridge, 2010), pp. 1–34.

Van der Hoven, I., "Power spectrum of horizontal wind speed in the frequency range from 0.0007 to 900 cycles per hour," J. Meteorol. **14**, 160–164 (1957).

Verrier, S., De Montera, L., Barthès, L., and Mallet, C., "Multifractal analysis of African monsoon rain fields, taking into account the zero rain-rate problem," J. Hydrol. **389**, 111–120 (2010).

Verrier, S., Mallet, C., and Barthès, L., "Multiscaling properties of rain in the time domain, taking into account rain support biases," J. Geophys. Res. **116**, D20119, doi:10.1029/2011JD015719 (2011).